Dust Coagulation Regulated by Turbulent Clustering in Protoplanetary Disks

Dust Coagulation Regulated by Turbulent Clustering in Protoplanetary Disks

Takashi Ishihara[1] , Naoki Kobayashi[2], Kei Enohata[2], Masayuki Umemura[3], and Kenji Shiraishi[4]
[1] Graduate School of Environmental and Life Science, Okayama University, Okayama 700-8530, Japan; ishihara@ems.okayama-u.ac.jp
[2] Department of Computational Science and Engineering, Graduate School of Engineering, Nagoya University, Nagoya 464-8603, Japan
[3] Center for Computational Sciences, University of Tsukuba, Tsukuba 305-8577, Japan; umemura@ccs.tsukuba.ac.jp
[4] Institute of Materials and Systems for Sustainability, Nagoya University, Nagoya 464-8601, Japan

Abstract

The coagulation of dust particles is a key process in planetesimal formation. However, the radial drift and bouncing barriers are not completely resolved, especially for silicate dust. Since the collision velocities of dust particles are regulated by turbulence in a protoplanetary disk, turbulent clustering should be properly treated. To that end, direct numerical simulations (DNSs) of the Navier–Stokes equations are requisite. In a series of papers, Pan & Padoan used a DNS with Reynolds number $Re \sim 1000$. Here, we perform DNSs with up to $Re = 16,100$, which allow us to track the motion of particles with Stokes numbers of $0.01 \lesssim St \lesssim 0.2$ in the inertial range. Through the DNSs, we confirm that the rms relative velocity of particle pairs is smaller by more than a factor of two, compared to that by Ormel & Cuzzi. The distributions of the radial relative velocities are highly non-Gaussian. The results are almost consistent with those by Pan & Padoan or Pan et al. at low Re. Also, we find that the sticking rates for equal-sized particles are much higher than those for different-sized particles. Even in the strong-turbulence case with α-viscosity of 10^{-2}, the sticking rates are as high as $\gtrsim 50\%$ and the bouncing probabilities are as low as $\sim 10\%$ for equal-sized particles of $St \lesssim 0.01$. Thus, turbulent clustering plays a significant role in the growth of centimeter-sized compact aggregates (pebbles) and also enhances the solid abundance, which may lead to the streaming instability in a disk.

Key words: hydrodynamics – methods: numerical – planets and satellites: formation – protoplanetary disks – turbulence

1. Introduction

Planetesimals are thought to be the precursors of both Earth-like planets and the cores of gas giants and ice giants. The formation of planetesimals has been a longstanding and perplexing obstacle toward the full understanding of the origins of planets. Planetesimals are widely believed to form as a consequence of the hierarchical coagulation from submicron-size dust particles to kilometer-size bodies in protoplanetary disks (e.g., Lissauer 1993; Chiang & Youdin 2010; Johansen et al. 2014). The growth, however, faces several difficulties, such as bouncing, fragmentation, and radial drift barriers. As the gas disk is partially pressure-supported in the radial direction, the gas rotates with a sub-Keplerian velocity. The resultant friction by the gas forces dust particles to drift toward the central star. In particular, the centimeter- to meter-size particles have large drift velocities and may rapidly fall into the central star on a timescale of a few hundred years (Adachi et al. 1976; Weidenschilling 1977), which is often referred to as the meter-size problem. Therefore, the growth timescale is required to be shorter than the drift timescale for the successful formation of planetesimals. However, as the dust particles grow, they become less sticky, and the high-velocity collisions may lead to bouncing or fragmentation instead of coagulation (Blum & Wurm 2008; Brauer et al. 2008a, 2008b; Birnstiel et al. 2009, 2012; Güttler et al. 2010; Zsom et al. 2010, 2011; Windmark et al. 2012).

The streaming instability is a potential mechanism to circumvent radial drift barriers (Youdin & Goodman 2005). In order for this instability to work successfully, the formation of centimeter-size compact aggregates (pebbles) and the enhancement of solid abundance in a protoplanetary disk are crucial (Johansen et al. 2009; Bai & Stone 2010; Johansen et al. 2014; Carrera et al. 2015; Ida & Guillot 2016; Yang et al. 2017). On the other hand, in recent years, *N*-body molecular dynamics simulations have shown that fluffy dust aggregates have the potential to overcome these bouncing or fragmentation barriers (Paszun & Dominik 2009; Wada et al. 2009; Meru et al. 2013; Seizinger & Kley 2013; Wada et al. 2013; Gunkelmann et al. 2016). Wada et al. (2013) derived the critical collision velocity u_c below which fluffy dust aggregates can coalesce: $u_c \simeq 60$–$80\,\mathrm{m\,s^{-1}}$ for ice dust and $u_c \simeq 6$–$8\,\mathrm{m\,s^{-1}}$ for silicate dust. This implies that icy aggregates, compared to silicate aggregates, overcome fragmentation barriers more easily.

Protoplanetary disks inevitably become turbulent due to differential rotation, and therefore the collision velocities are regulated by turbulent motion in a wide range of particle sizes, from 1 mm to 10 m (e.g., see the review by Johansen et al. 2014). Völk et al. (1980) built up a framework set (the Völk-type model) based on a Langevin approach for the nonlinear response of dust particles to turbulent eddy motion, which was further developed by Markiewicz et al. (1991). Ormel & Cuzzi (2007, hereafter OC07) provided closed-form analytical approximations to the Völk-type model. Okuzumi et al. (2012), based on an analytic formula by OC07, have simulated the growth of fluffy icy aggregates outside the snow line, taking into account the change in aggregate porosities, and found that the porosity evolution enables the icy aggregates to grow

across the radial drift barrier. Kataoka et al. (2013) have explored the compression of fluffy aggregates and shown that the aggregates can evolve into compact icy planetesimals. The abovementioned works revealed that icy planetesimals can form in a wide range beyond the snow line in protoplanetary disks. However, the difficulties for silicate planetesimal formation are difficult to alleviate, because the critical collision velocity for silicate dust is smaller than that for icy dust by an order of magnitude.

The actual sticking rates of dust particles are strongly dependent on the probability distribution function (PDF) of the collision velocities. Even if the root mean square (rms) collision velocity exceeds the critical value, a subset of the dust particles can have collision velocities lower than the critical one and eventually grow, evading the fragmentation barrier. Employing the rms collision velocity derived by OC07, Windmark et al. (2012) and Garaud et al. (2013) explored the effects of the PDF on the collisional dust growth barriers, under the assumption of a Gaussian (Maxwellian) distribution. However, the PDFs of turbulence-induced relative velocities have been found to be highly non-Gaussian by numerical, experimental, and theoretical studies (Sundaram & Collins 1997; Gustavsson et al. 2008; Gustavsson & Mehlig 2011; Hubbard 2012). In addition, it is known that particles with small inertia preferentially concentrate in low-vorticity, high-strain regions during turbulence due to the centrifugal mechanism of the vorticity (Maxey 1987; Squires & Eaton 1991; Fessler et al. 1994). Furthermore, effects such as "caustics" (Wilkinson et al. 2006) and the "sling effect" (Falkovich & Pumir 2007) allow the particles with large inertia to become less coupled to the local fluid velocity field and to assemble from different regions (e.g., see Bragg & Collins 2014). Such "turbulent clustering" effects are significant when considering the process of collisional coagulation of dust particles in protoplanetary disks.

To treat turbulent clustering properly, the direct numerical simulation (DNS) of the Navier–Stokes (NS) equations coupled with tracking dust particle motions are requisite. In the DNS, the smallest eddies in the turbulence are resolved without introducing numerical viscosity and turbulence models. Pan et al. (2011) handled the collision statistics with turbulent clustering, using an Eulerian formulation instead of the NS equations. Then, in a series of the papers by Pan & Padoan (2013, hereafter PP13), Pan et al. (2014a, 2014b), Pan & Padoan (2014), and Pan & Padoan (2015, hereafter PP15), a DNS of the NS equations in the context of planetesimal formation was used. By analyzing the DNS data, they studied the statistics of colliding dust grains including the radial relative velocity, its probability distribution, and the collision rate between dust grains. However, the Reynolds number dependence of the results has not been investigated yet.

The motion of particles in turbulence is characterized by the Stokes number given by $St = \Omega \tau_{\mathrm{p}}$, where Ω is the Keplerian frequency at a radial distance and τ_{p} is the stopping time due to the gas friction. In addition, another Stokes number can be defined by the turnover timescale τ_η of the smallest eddies of turbulence as $St_\eta = \tau_{\mathrm{p}}/\tau_\eta$. St_η is determined by the resolution of the simulations and follows relation $St_\eta/St \propto Re^{1/2}$, where Re is the Reynolds number. According to Kolmogorov theory, as the Reynolds number increases, the inertial range of turbulence that regulates the particle dynamics becomes wider.

The scale ratio between the largest and the smallest eddies is known to increase in proportion to $Re^{3/4}$.

Considering the molecular viscosity of a protoplanetary disk, the Reynolds number is estimated to be as high as $Re = 10^{10}(\alpha/10^{-2})(R/\mathrm{au})^{-3/2}$ in the Minimum-mass Solar Nebula (MMSN) Model (Hayashi 1981), where α is the turbulence parameter and R is the radial distance from the central star. However, even if the Reynolds number is smaller than this value, we can trace the particle behavior over a range of Stokes numbers according to the simulated inertial range of turbulence. If we focus on particle sizes from millimeters to meters, simulations of $Re > O(10^4)$ are required. In the simulations by PP13, the resolution was $Re \simeq 10^3$, which corresponds to $St_\eta/St = 23.5$ and realizes the inertial range of turbulence over only one order of magnitude in linear dimensions. However, a recent development in supercomputers allows us to perform particle tracking simulations based on the DNS at Reynolds numbers as high as $Re > O(10^4)$ (Ishihara et al. 2015)

In this paper, we perform high Reynolds number DNSs, where the number of grid points and the Reynolds number are up to $N^3 = 2048^3$ and $Re = 16{,}100$, respectively, which corresponds to $St_\eta/St = 85$ and can realize the inertial range over two order of magnitude in linear dimensions. Through these DNSs, we obtain the rms relative velocity for particle pairs and the PDF of the collision velocities. We find that the rms relative velocity is smaller than that derived by the Völk-type model developed by OC07. In addition, we discuss the growth timescale of dust aggregates and the sticking rates in the context of overcoming the drift and fragmentation barriers.

In Section 2, we present the method of our particle tracking simulation, based on the DNS of forced incompressible homogeneous isotropic turbulence. The statistics of the motion of the particles obtained by the DNS are shown in Section 3. The statistics include the rms relative velocity, the collision kernel, and the PDF of the radial relative velocities. The results are compared to the Völk-type model of OC07. In Section 4, assuming the MMSN model, we assess the collision timescale for both compact and fluffy aggregates and the sticking rates of dust particles. Our conclusions are summarized in Section 5.

2. Particle Tracking Using DNS of Turbulence

2.1. DNS of Forced Incompressible Turbulence

In protoplanetary disks, the turbulence is known to be subsonic and thus essentially incompressible (Hayashi 1981). Therefore, in this paper, we consider the three-dimensional turbulence of an incompressible fluid of unit density that obeys the NS equations

$$\frac{\partial \boldsymbol{u}}{\partial t} + (\boldsymbol{u} \cdot \nabla)\boldsymbol{u} = -\nabla p + \nu \nabla^2 \boldsymbol{u} + \boldsymbol{f} \qquad (1)$$

and the continuity equation

$$\nabla \cdot \boldsymbol{u} = 0, \qquad (2)$$

where $\boldsymbol{u}$, p, ν, and $\boldsymbol{f}$ are the velocity, pressure, kinematic viscosity, and external force, respectively. The numerical method used in the DNS is essentially identical to that used in Yokokawa et al. (2002), Kaneda et al. (2003) and Ishihara et al. (2016), which is briefly reviewed here for convenience. (The readers may refer to Yokokawa et al. 2002 and Ishihara et al. 2015 for details of the parallel computations.) In the DNS,
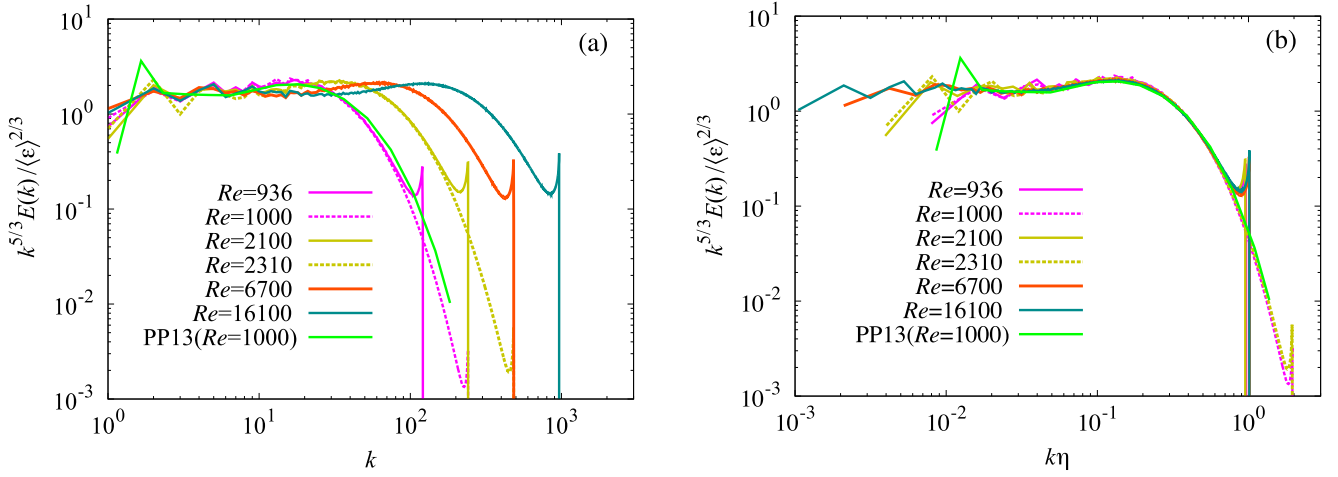
Figure 1. Compensated energy spectra of the turbulence, $k^{5/3}E(k)/\langle\varepsilon\rangle^{2/3}$, for different Reynolds numbers Re, as a function of (a) k and (b) $k\eta$. The data from Pan & Padoan (2013, PP13 in the panels) are also plotted for comparison.

Table 1
Simulation (DNS) Parameters and Turbulence Characteristics

Run	N^3	Re	k_{max}	$\Delta t(\times 10^{-3})$	$\nu(\times 10^{-4})$	L	$\eta(\times 10^{-3})$	T	τ_η
256-1	256^3	936	121	1.0	7.0	1.13	7.97	1.96	0.091
512-1	512^3	2100	241	1.0	2.8	1.02	3.95	1.77	0.056
1024-1	1024^3	6710	471	0.625	1.1	1.28	2.10	2.21	0.040
2048-1	2048^3	16,100	732	0.4	0.44	1.23	1.05	2.13	0.025
512-2	512^3	1000	241	1.0	7.0	1.10	8.10	2.21	0.094
1024-2	1024^3	2310	483	0.625	2.8	1.21	4.03	1.94	0.058

Note. $Re = u'L/\nu$, $T = L/u'$, and $\tau_\eta \equiv (\nu/\langle\varepsilon\rangle)^{1/2}$.

the NS equations are solved by a fully alias-free Fourier spectral method, where aliasing errors are removed by the so-called phase-shift method. (Note that the Fourier spectral method gives the spatial derivatives to spectral accuracy and is not subject to the numerical viscosity. On the other hand, in finite difference schemes, the spatial derivatives are calculated to finite accuracy, and the numerical viscosity is inevitably included). The computation domain is assumed to be 2π periodic in each Cartesian coordinate direction, so that both the minimum wavenumber and the wavenumber increment in the DNS are unity. The maximum wavenumber is given by $k_{max} = \sqrt{2}N/3$, where N is the number of grid points in each of the Cartesian coordinates in real space. Time integration is achieved using a fourth-order Runge–Kutta method with a constant time increment.

The forcing $\boldsymbol{f}$ that generates turbulence is given by $\hat{\boldsymbol{f}}(\boldsymbol{k}) = -c\hat{\boldsymbol{u}}(\boldsymbol{k})$ in the wave-vector space, where $\hat{\boldsymbol{f}}$ and $\hat{\boldsymbol{u}}$ are Fourier transforms of $\boldsymbol{f}$ and $\boldsymbol{u}$, respectively. The value of c is set to be non-zero only in the wavenumber range of $k < 2.5$ and is adjusted at every time step so as to keep the total kinematic energy, $E \equiv 3u'^2/2 = U^2/2$, almost time independently (≈ 0.5). Here, u' is the rms value of the fluctuating velocity in one direction and $U = \langle\boldsymbol{u}\cdot\boldsymbol{u}\rangle^{1/2}$ is the three-dimensional (3D) rms of the flow velocity $\boldsymbol{u}$. A similar forcing was used in Kerr (1985), Vincent & Meneguzzi (1991), and Jimenez et al. (1993). The integral length scale L and the eddy turnover time T are defined as $L = \pi/(2U^2)\int_0^k E(k)/k\,dk$ and

$T = L/U$, respectively. T corresponds to Ω^{-1} in actual dimensions. The variations of L and T in steady turbulence generated by the forcing are within 10% of the mean (Ishihara et al. 2007).

We use the velocity fields obtained by the DNS in Kaneda et al. (2003) and Ishihara et al. (2007) as the initial conditions for the present study and adopt the same values for the kinematic viscosity. Therefore, each velocity field at $t = 0$ is in a statistically steady state of turbulence, and we do not have any initial transient period in the turbulence field used in the particle tracking simulation. The details of the turbulence characteristics of the DNS data are found in Ishihara et al. (2007).

In Table 1, we show a summary of the DNS parameters and turbulence characteristics. In the DNSs, the value of ν is chosen so that $k_{max}\eta = 1$ or 2, where η is the Kolmogorov micro-length scale given by $\eta = (\nu^3/\langle\varepsilon\rangle)^{1/4}$ with the mean energy dissipation rate $\langle\varepsilon\rangle$. The value of $k_{max}\eta$ represents a small-scale resolution. Each "Run" in Table 1 is named by the combination of the values of N and $k_{max}\eta$. It is known that the sensitivity/insensitivity to the values of $k_{max}\eta$ depends on the statistical quantity to be studied (Yamazaki et al. 2002; Schumacher 2007; Watanabe & Gotoh 2007; Donzis et al. 2008; Yeung et al. 2015). It will be shown that the collision statistics are not that sensitive to the $k_{max}\eta$ values, provided that $k_{max}\eta \gtrsim 1$.

Figure 1 shows the compensated energy spectra, $k^{5/3}E(k)/\langle\varepsilon\rangle^{2/3}$, of the generated turbulence for different values of Re and $k_{max}\eta$. The spectrum of the velocity field used in PP13 and PP15 is also shown for comparison. The horizontal range
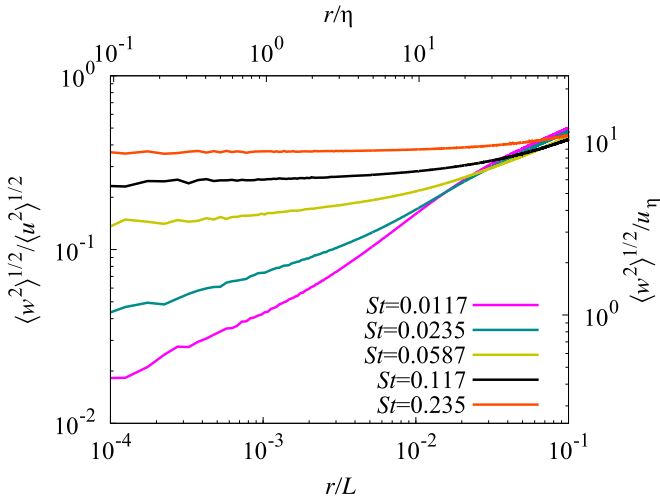
Figure 2. rms relative velocity as a function of the separation (r) between a pair of particles. The data are plotted for each St number for 512^3 particles at $t = 3T$ in the DNS of Run 2048-1 ($Re = 16,100$) and normalized by $\langle u^2 \rangle^{1/2} \equiv \langle \boldsymbol{u} \cdot \boldsymbol{u} \rangle^{1/2}$ or u_η.

corresponds to the "inertial range," where $E(k) \propto k^{-5/3}$. In Figure 1, we observe that the horizontal range becomes wider with increasing Re. Therefore, it is expected that the inertial range may be satisfactorily resolved by our DNS. In the DNS of $Re = 16,100$, we realize $L/\eta = 1.2 \times 10^3$ and $T/\tau_\eta = 85$, respectively, which are much larger than $L/\eta = 1.4 \times 10^2$ and $T/\tau_\eta = 23.5$ for $Re = 1000$.

We recognize that the compensated energy spectra obtained by our DNSs have a pile-up near $k = k_{max}$. It is known that such a pile-up is caused by the wavenumber truncation in the DNS based on a Fourier spectral method. It is also known that such a pile-up does not appear in the turbulence simulation using finite difference methods. Therefore, the difference between our spectra and the spectra of PP13 and PP15 near $k = k_{max}$ comes from the difference in the numerical methods.

To see the effect of the wavenumber truncation on the Fourier spectral method, we compare the energy spectra between runs 512-1 and 1024-2 (and also between runs 256-1 and 512-2) in Figure 1. They are slightly different from each other in the low wavenumber range ($k < 3$) and in the high wavenumber range ($k\eta > 0.7$). The difference in the low wavenumber range is presumably caused by the difference in the energy-containing eddies at the forcing scales, while the difference at high wavenumbers is caused by the wavenumber truncation. Note that in contrast to the high and low wavenumber ranges, the difference between the spectra in the intermediate range for the two runs is very small. This comparison suggests that the collision statistics are not sensitive to the difference between $k_{max}\eta \sim 1$ and $k_{max}\eta \sim 2$, if they are insensitive to the detail of the fine-scale statistics in the energy dissipation range of the turbulence. In this study, we will mainly present the results obtained using the DNS data with $k_{max}\eta \sim 1$. However, we will also show the results of the DNS data with $k_{max}\eta \sim 2$ to confirm the insensitivity of the quantity to small-scale resolution (see Figures 3 and 10).

2.2. Particle Tracking Simulation

We consider the motion of small solid particles with density ρ_s in a gas flow with density ρ_g. The ratio $\beta = \rho_s/\rho_g$ is assumed to be much larger than unity. Then, the equation of motion of each inertial particle is given by

$$\frac{d\boldsymbol{X}}{dt} = \boldsymbol{V}, \quad \frac{d\boldsymbol{V}}{dt} = \frac{1}{\tau_p}(\boldsymbol{u} - \boldsymbol{V}), \quad (3)$$

where $\boldsymbol{X}, \boldsymbol{V}$, and τ_p are the position, velocity, and stopping time of the particle, respectively, and $\boldsymbol{u}$ is the velocity of the fluid flow at $\boldsymbol{X}$ (see, e.g., Davila & Hunt 2001). Equation (3) is solved with the fourth-order Runge–Kutta method, where the time step (Δt) is set to be twice as large as that used to solve Equation (1) (because we need $\boldsymbol{u}(\boldsymbol{x}, n\Delta t/2)$ in this scheme). The velocity $\boldsymbol{u}$ at the particle position is evaluated by using an interpolation method. To obtain accurate statistics, we use cubic spline interpolation (see Yeung & Pope 1988). The interpolation scheme is implemented by solving tridiagonal matrix problems in parallel with the method developed by Mattor et al. (1995). See Ishihara et al. (2015) for the actual parallel implementation.

In this paper, we normalize Equation (3) in two ways. One is by using L and T, and the other is by using η and $\tau_\eta \equiv (\nu/\langle\varepsilon\rangle)^{1/2}$. In the former, the motion of the particles is characterized by the Stokes number given by $St = \tau_p/T$, and in the latter, the motion is characterized by another Stokes number, given by $St_\eta = \tau_p/\tau_\eta$. Note that $St_\eta/St = T/\tau_\eta \propto Re^{1/2}$. In the case of a typical protoplanetary disk of $Re = O(10^{10})$, the ratio is $O(10^5)$. However, even if the Reynolds number is smaller than this value, we can trace the particle behavior over a range of Stokes numbers according to the simulated inertial range of the turbulence. In our largest DNS of $Re = 16,100$, the value of St_η/St is 85.

In our particle tracking simulation, we set seven different values for St as follows:

$$St = 0.00158, \ 0.00632, \ 0.0158, \ 0.0316,$$
$$0.0632, \ 0.158, \ 0.316, \ \text{for } N = 512, \quad (4)$$

$$St = 0.00188, \ 0.0038, \ 0.0094, \ 0.0188,$$
$$0.038, \ 0.094, \ 0.188, \ \text{for } N = 1024, \quad (5)$$

$$St = 0.00117, \ 0.00587, \ 0.0117, \ 0.0234,$$
$$0.0587, \ 0.117, \ 0.234, \ \text{for } N = 2048. \quad (6)$$

The corresponding values of $St_\eta = St(T/\tau_\eta)$ are 0.1, 0.2, 0.5, 1, 2, 5, and 10 for $N = 512$, 1024 and 0.1, 0.5, 1, 2, 5, 10, and 20 for $N = 2048$.

For each value of St, we track a maximum of 512^3 particles. The particles are distributed randomly in the whole computational domain at $t = 0$ with initial velocity $\boldsymbol{V}_0 = 0$. The statistics related to the particle motions are taken at $t = 3T$ in the following analyses. By performing several preliminary runs, we have confirmed that the particle statistics become almost time independent after $t = 3T$.

In this paper, we focus on the particles with Stokes number less than 0.3. The collision statistics of particles with $St = O(0.1)$ are expected to be mainly affected by the eddies in the inertial range that are able to be simulated properly by high-resolution DNSs of homogeneous isotropic turbulence using appropriate forcing methods. Therefore, the aim of this paper is to provide reliable results of the collision statistics of the particles in the inertial range by performing a series of high-resolution DNSs. Since the relative velocity attains its maximum at $St \sim 1$, such collisions may be important to discuss the fragmentation barrier. However, it is also true that
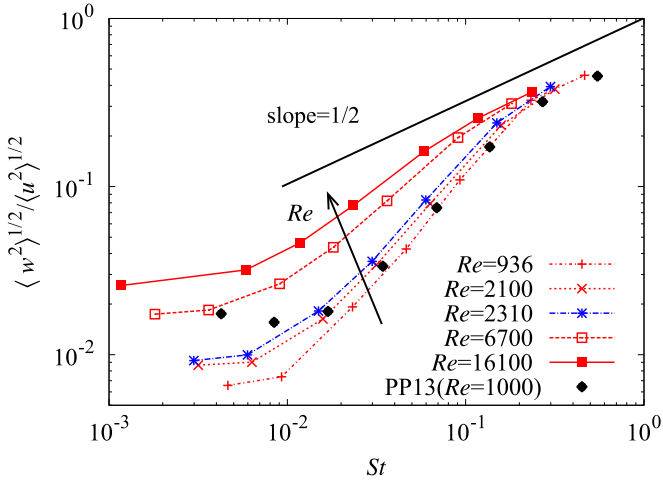
Figure 3. rms relative velocity at $r = 10^{-3}L$ as a function of the St number. The dependence on the Re numbers is shown for $Re = 936$ (dotted–dashed line), $Re = 2100$ (dotted line), $Re = 2310$ (chain line), $Re = 6700$ (dashed line), and $Re = 16,100$ (solid line). The data from PP13 ($Re = 1000$, $r = \eta/4 \sim 2 \times 10^{-3}L$) are also plotted for comparison.

Figure 4. rms relative velocity at $r = \eta/4$ for particle pairs with fixed Stokes ratios, $f \equiv St_2/St_1 = 1$, $1/2$, $1/5$, and 0, where $f = 1$ corresponds to the monodisperse case and $f = 0$ to the relative velocities against the turbulent flow itself. The data are obtained at $t = 3T$ in Run 2028-1 ($Re = 16,100$).

such collisions occur via the processes of collision and sticking of the dusts with smaller values of St, which are dominated by eddies in the inertial range. Therefore, we took a bottom-up approach.

3. Numerical results

3.1. Relative Velocity

The relative velocity between a pair of particles with a separation r and its rms value are calculated at locations X_1 and X_2 as $w = V_1 - V_2$ and

$$\langle w^2 \rangle^{1/2} = \left\{ \frac{1}{N_p} \sum_{|X_1 - X_2| = r} w^2 \right\}^{1/2}, \qquad (7)$$

respectively, where V_1 and V_2 are the velocities of the particles and N_p is the number of pairs. Figure 2 shows the r dependence of the rms relative velocity between equal-sized particles. Actually, collision velocities should be measured at particle sizes, which are in general much smaller than the Kolmogorov length scale in turbulence in protoplanetary disks. To estimate the rms relative velocity at a separation of less than $\eta/4$ in the DNSs, one may need a much larger number of particles than that used in our DNSs. However, Figure 2 demonstrates that the relative velocity for the particles of $St > 0.05$ is not significantly affected by eddies smaller than $\eta(\sim 10^{-3}L)$ and therefore almost constant at a separation $r \lesssim 10^{-3}L$.

Figure 3 presents the St dependence of the rms relative velocity at a fixed small separation of $r = 10^{-3}L$ for different Reynolds numbers. Here, $r/L = 10^{-3}$ approximately corresponds to $r/\eta = 1/8$, $1/4$, $1/2$, and 1 for runs at $Re = 936$, 2100 (and 2310), 6700, and $16,100$, respectively. (The other comparison for different Re values using a fixed separation of r/η would also be possible. However, here we are interested in the $St(=\tau_p/T)$ dependence of the rms relative velocity. So, we measure the relative velocity using a fixed small separation r normalized by L). The data from PP13 ($Re = 1000$, $r = \eta/4$) agree well with our data ($Re = 936$, $r = \eta/8$) in the range of large St ($\gtrsim 0.1$).
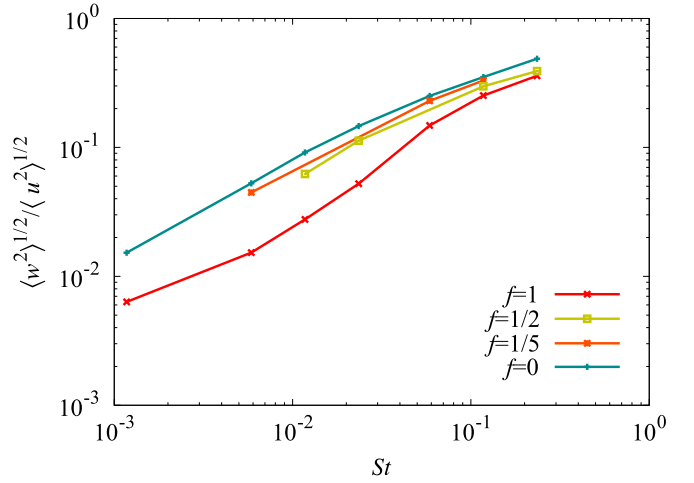
They deviate from our results in the range $St \lesssim 10^{-2}$. This deviation is presumably due to the difference in the value of r/η and comes from the range of $St_\eta < 1$. However, in this paper, we focus on the collision statistics in the range $St_\eta > 1$. In addition, the data for $Re = 2100$ ($k_{max}\eta = 1$) agree well with the data for $Re = 2300$ ($k_{max}\eta = 2$). This agreement indicates that the relative velocities at small separations are not so sensitive to the difference in the value of $k_{max}\eta$.

In Figure 3, we perceive that the relative velocity at the small separation of $r/L = 10^{-3}$ is an increasing function of Re for a fixed value of St. Also, we observe that the curves tend to approach a line with slope $1/2$ at the portion with larger values of St ($\gtrsim 0.1$) for $Re > 10^4$. This dependence ($\langle w^2 \rangle^{1/2} \propto St^{1/2}$) is consistent with the inertial range scaling of the relative velocity in Völk-type models; see PP15.

3.2. Bidisperse Case

In the above, we considered the monodisperse case of identical particles. Here, we present the results for bidisperse cases, i.e., the relative velocities of particles with different St numbers (St_1 and St_2). Figure 4 shows the $St(= St_1)$ dependence of the rms relative velocity between particles with different ratios of $f \equiv St_2/St_1$. To compare the relative velocities at the scale of the smallest eddies, we show the results at $r = \eta/4$. We find that the rms relative velocity is higher for the different-sized particles than for the equal-sized particles. This trend is prominent for $St \approx 10^{-2}$. The result can be understood by considering that the equal-sized particles with small separations move in the same way in a turbulent flow, and therefore the relative velocities remain low.

It is known that collisions between particles at high speeds may lead to bouncing or fragmentation. Therefore, the sticking rate of collision particles depends on the statistics of relative velocities. The present results suggest that collisions between identical particles are more appropriate for sticking than collisions between particles of different sizes. We will discuss the sticking rate quantitatively in Section 4.

3.3. Comparison with the Völk-type Model

As for the relative velocities of particles induced by turbulence, a closed-form expression developed by OC07 has been widely adopted (e.g., see the review by Johansen et al. 2014). The original formalism (the Völk-type model) was developed by Völk et al. (1980) and Markiewicz et al. (1991). Cuzzi & Hogan (2003) obtained closed-form expressions for the Völk-type model. OC07 generalized the approach and results of Cuzzi & Hogan (2003) to obtain closed-form expressions for relative velocities between particles of arbitrary, and unequal, sizes.

For equal-size particles with a stopping time of τ_p, the closed-form expression (OC07) is given by

$$\langle w^2 \rangle = \int_{k^*}^{\infty} 4E(k)(1 - F(k)^2)dk, \quad (8)$$

where $F(k) = \tau_p/(\tau_p + \tau_k(k))$, $\tau_k(k) = [2E(k)k^3]^{-1/2}$, and the critical wavenumber k^* for the particle with stopping time τ_p is determined by

$$\frac{1}{\tau_p} = \frac{1}{\tau_k(k^*)} + k^* v_{rel}(k^*), \quad (9)$$

where the relative velocity v_{rel} between a particle and an eddy is given by

$$v_{rel}^2(k^*) = \int_{k_L}^{k^*} 2E(k')[\tau_p/(\tau_p + \tau_k(k'))]^2 dk' \quad (10)$$

and k_L is the smallest wavenumber. OC07 assumed the energy spectrum given by

$$E(k) = \begin{cases} V_g^2/(3k_L)(k/k_L)^{-5/3} & \text{for } k_L < k < k_\eta, \\ 0 & \text{for } k < k_L, k > k_\eta, \end{cases} \quad (11)$$

for which the total energy is $V_g^2/2$. As shown in PP15, in turbulent flows with a wide inertial range, the above model predicts a $\tau_p^{1/2}$ scaling for $\langle w^2 \rangle^{1/2}$, if τ_p is in the inertial range.

In Figure 5, we compare the DNS results of the relative velocity with the Völk-type model given by Equation (8) in which Equation (11) is used for $E(k)$ by setting $k_\eta/k_L = Re^{4/3}$ and $Re = 10^8$. For comparison, the Völk-type models that tentatively employ the DNS data for $E(k)$ in Equation (8) are also plotted. In the range $St = O(0.1)$, the latter models agree well with the Völk-type model that assumes the model spectrum (11). We recognize that the DNS results for $Re = 16,100$ has a slope of $1/2$ for $0.05 \lesssim St \lesssim 0.2$. The slope is consistent with the Völk-type model for high-Re turbulence. However, the DNS values are smaller than those of the Völk-type model by a factor of two. PP15 did not show a clear slope of the relative velocity, but their result suggested that the Völk-type models typically overestimate the rms of the particle relative velocity. Our results suggest that in the inertial range of high-Re turbulence, the rms of the particle relative velocity obeys the scaling law, but the values are smaller than those of the Völk-type model by a factor of two. PP15 proposed an improved closed expression of the relative velocity (their Equation (25)) and an improved formula of Völk-type models (at their Figure 10). We plot these expressions in Figure 5 for comparison. The difference between the former and the Völk-type model by OC07 is small. On the other hand, the latter formula seems to work well at $St \gtrsim 0.1$.

In Figure 6, we compare the DNS results of the relative velocities to those of the closed-form expression derived
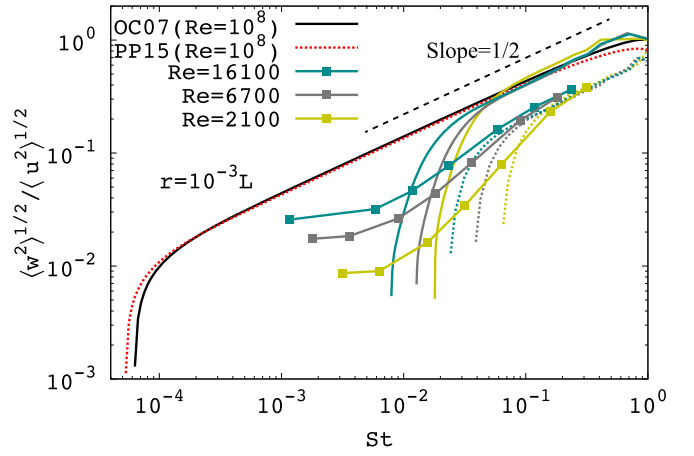

Figure 5. rms relative velocity at $r = 10^{-3}L$ is compared to the Völk-type model. Colored dashed lines with points represent the DNS results at $t = 3$ T for $Re = 2100$ (yellow), $Re = 6700$ (gray), and $Re = 16,100$ (cyan). Colored lines denote the Völk-type model employing $E(k)$ in the DNSs. The black line shows the Völk-type model by OC07. The red dotted line shows an improved closed expression by PP15 (their Equation 25). Colored dotted lines show an improved formula of the Völk-type models presented in PP15 (their Figure 10).
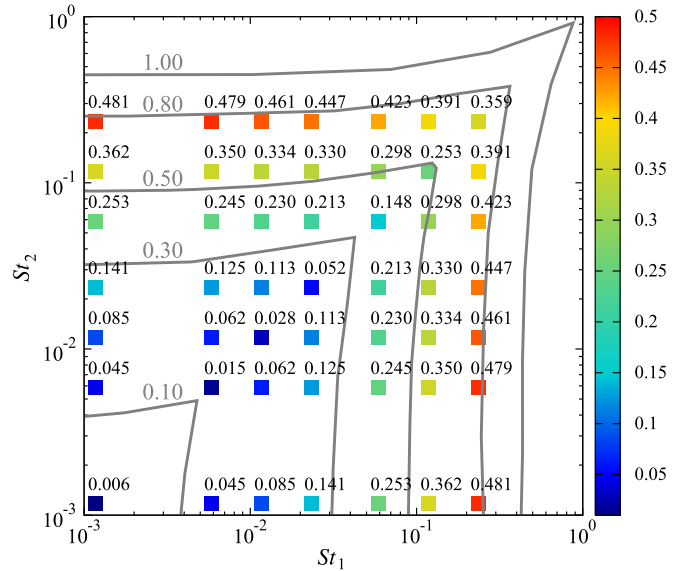

Figure 6. Turbulence-induced rms relative velocities $\langle w^2 \rangle^{1/2}$ normalized to $\langle u^2 \rangle^{1/2}$ between two particles characterized by St_1 and St_2. Colored squares (with rms values) represent the DNS results for a particle separation of $r = \eta/4$ at $t = 3T$ ($Re = 16,100$). Gray contours (with attached rms values) denote the prediction of the Völk-type model (12), which is equivalent to Figure 4(C) of OC07. The diagonal line ($St_1 = St_2$) corresponds to Figure 5. Note that the DNS results for St_1 (or St_2) <0.05 are more or less affected by viscosity.

by OC07. The DNS results for $Re = 16,100$ are shown by colored squares with rms values as functions of $St_1 = \tau_1/t_L$ and $St_2 = \tau_2/t_L$. For unequal-sized particles with stopping times of τ_1 and τ_2, the closed-form expression (OC07) is given by

$$\langle w^2 \rangle = \frac{V_g^2}{t_L}\left(\left[\tau_k + \frac{\tau_1^2}{\tau_1 + \tau_k}\right]_{\tau_k=t_\eta}^{\tau_k=\max(\tau_1^*,\tau_2^*)} \right.$$

$$+ \frac{\tau_2 - \tau_1}{\tau_1 + \tau_2}\left[\frac{\tau_1^2}{\tau_1 + \tau_k}\right]_{\tau_k=\max(\tau_1^*,\tau_2^*)}^{\tau_k=t_L}$$

$$\left. + (1 \leftrightarrow 2)\right), \quad (12)$$

where $t_L = (V_L k_L)^{-1}$, $V_L^2 = (2/3)V_g^2$, and $t_\eta = Re^{-1/2} t_L$. τ_1^* and τ_2^* are the solutions of Equation (9) for $\tau_p = \tau_1$ and $\tau_p = \tau_2$, respectively. The relative velocity variance $\langle w^2 \rangle^{1/2}$ of this formula is shown by contours in Figure 6 for the case $Re = 10^8$. The comparison with the relative velocities obtained by the DNS clarifies that the DNS results are smaller than half of the values of the closed-form expression given by OC07, regardless of the St ratios. In particular, for equal-sized particles with $St \lesssim 10^{-2}$, the DNS results are smaller by an order of magnitude. These reduced relative velocities have a significant impact on avoiding the fragmentation barrier, which is discussed in detail in Section 4.

3.4. Collision Kernel

So far, we have focused on the variance of relative velocities, which gives a measure of the collision rate. Here, we consider the collision kernel to incorporate the turbulent clustering effect properly. The collision rate per unit volume between two particles with radii a_1 and a_2 can be expressed as

$$n_1(a_1)n_2(a_2)\Gamma(a_1, a_2), \quad (13)$$

where $n_1(a_1)$ and $n_2(a_2)$ are the average number densities and $\Gamma(a_1, a_2)$ is the collision kernel. The kernel formula hitherto used in dust coagulation models is $\Gamma^{\text{com}} = \pi d^2 \langle w^2 \rangle^{1/2}$ with $d = a_1 + a_2$, where the effect of turbulent clustering is not taken into account and the rms relative velocity, $\langle w^2 \rangle^{1/2}$, is usually taken from the model of Völk et al. (1980). As a statistical mechanical description of Γ for zero-inertia particles, Saffman & Turner (1995) proposed a spherical formulation, in which the kernel is given by $\Gamma = 2\pi d^2 \langle |w_r| \rangle$ with the radial relative velocity, $w_r = \mathbf{w} \cdot (\mathbf{X}_2 - \mathbf{X}_1)/|\mathbf{X}_2 - \mathbf{X}_1|$. In addition, Sundaram & Collins (1997) considered the turbulent clustering effect on Γ and derived an expression for finite-inertia particles. Wang et al. (2000) suggested that a formula (based on the spherical formulation),

$$\Gamma^{\text{sph}} = 2\pi d^2 \langle |w_r| \rangle g(d), \quad (14)$$

is more accurate than the formula considered by Sundaram & Collins (1997), where $g(d)$ is the radial distribution function (RDF) at $r = d$. The RDF is related to the two-point correlation function $\xi(r)$ by $g(r) = 1 + \xi(r)$, and evaluated by

$$g(r) = \frac{N(r)}{4\pi r^2 \bar{n} dr}, \quad (15)$$

where $N(r)$ is the average number of particles in a spherical shell of volume $4\pi r^2 dr$ at a distance r from a reference particle and $\bar{n}$ is the average particle number density. For a uniform distribution of particles, we have $g(r) = 1$, i.e., $\xi(r) = 0$. For a non-uniform distribution of particles due to turbulent clustering, we have $g(r) > 1$. Recently, Pan & Padoan (2014) and PP15 evaluated Γ^{sph} by performing the DNS with $Re = O(10^3)$ to study the effect of turbulent clustering on the collision kernel.

Here, we use our DNS data with Reynolds numbers up to $Re = 16,100$ to obtain $\langle |w_r| \rangle$ and $g(r)$, and to elucidate the Re dependence of the collision kernel. Figure 7 shows the normalized radial relative velocity, $2\langle |w_r| \rangle / \langle w^2 \rangle^{1/2}$, as a function of St for different Re numbers. As seen in this figure,
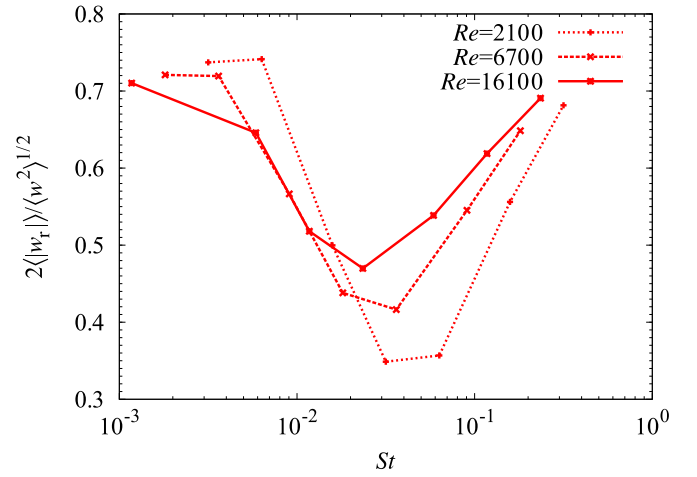

Figure 7. Averaged radial relative velocities $\langle |w_r| \rangle$ at $r = 10^{-3}L$, normalized by the relative velocity variance, as a function of the St number. Results are shown for $Re = 16,100$ (solid line), $Re = 6700$ (dashed line), and $Re = 2100$ (dotted line).

the values are always less than unity, and therefore the use of $\langle w^2 \rangle^{1/2}$ for the collision kernel leads to the overestimation. Additionally, since the values are a decreasing or increasing function of St, $\langle |w_r| \rangle$ does not obey the power law ($\propto St^{1/2}$) like $\langle w^2 \rangle^{1/2}$ does (Figure 3). Therefore, it is concluded that there are quantitative and qualitative discrepancies from $\langle w^2 \rangle^{1/2}$ for evaluating the collision kernel Γ. The low value of $\langle |w_r| \rangle$ leads to the enhancement of the particle sticking rates as discussed in Section 4. Pan & Padoan (2014) studied the St dependence of the ratio $2\langle |w_r| \rangle / \langle w^2 \rangle^{1/2}$ and showed that the values of the ratio approach its Gaussian value of $(8/3\pi)^{1/2} \simeq 0.92$ for $St > 1$. They argued that the non-Gaussianity peaks at $St_\eta \simeq 1$, resulting in a dip in the ratio at $St_\eta \simeq 1$. Figure 7 shows that the bottom position of the dip is around $St_\eta \simeq 1$–2, and therefore the dip becomes shallower accordingly as Re increases.

Figure 8 shows the St dependence of $g(r)$ in the DNS of Run 2048-1 ($Re = 16,100$). The behaviors of $g(r)$ are quantitatively consistent with the recent DNS results by Ireland et al. (2016). In Figure 8, we see that $g(r)$ is approximately constant at $r/L \lesssim 10^{-2}$ for $St \gtrsim 0.1$. This fact allows us to use the constant value when considering the collision statistics (as discussed in Section 4).

Figure 9 shows the St dependence of $g(r)$ at $r/L = 10^{-3}$ and $r/L = 10^{-2}$ for three different values of Re. Here, $r/L = 10^{-3}$ (10^{-2}) corresponds to $r/\eta = 1/4$ (5/2), 1/2 (5), and 1 (10) for $Re = 2100$, 6700, and 16,100, respectively. Figure 9 demonstrates that $g(r)$ has a peak for a fixed value of r. Also, Figure 8 suggests that the value of St at the peak depends on r, and $g(r)$ has a peak near $St_\eta = 1$ for small values of $r = O(\eta)$. In Figure 9, we notice that, for fixed values of $St = O(0.1)$ and r/L, $g(r)$ is a decreasing function of Re provided that $St_\eta \gtrsim 2.0$; this Re dependence is weaker for the larger values of St. We also observe that, for fixed values of $St = O(0.1)$ and Re, $g(r)$ becomes larger as r/L decreases; this r/L dependence is weaker for larger values of St (as shown in Figure 8). The Re dependence and r/L dependence of $g(r)$ suggest that an asymptotic behavior of $g(r)$ (in the range of $St = O(0.1)$) for much smaller r and for much higher Re can be surmised from the DNS data of $Re = O(10^4)$.
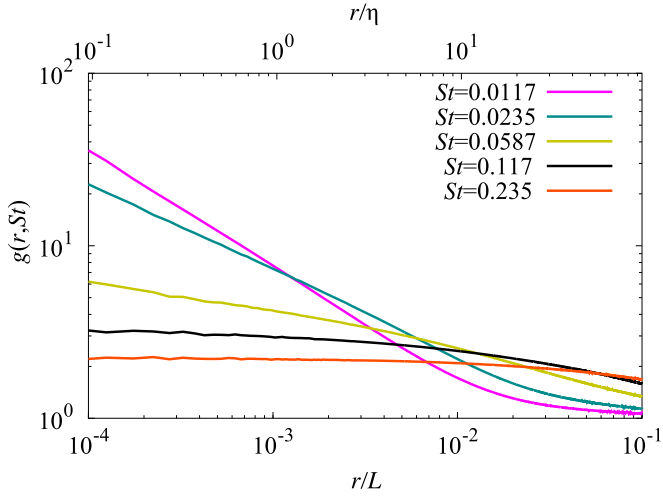
Figure 8. RDFs for particles with different St numbers; each value of St corresponds respectively to $St_\eta = 1$, 2, 5, 10, and 20. The used data are 512^3 particles at $t = 3T$ in the DNS of Run 2048-1 ($Re = 16,100$).
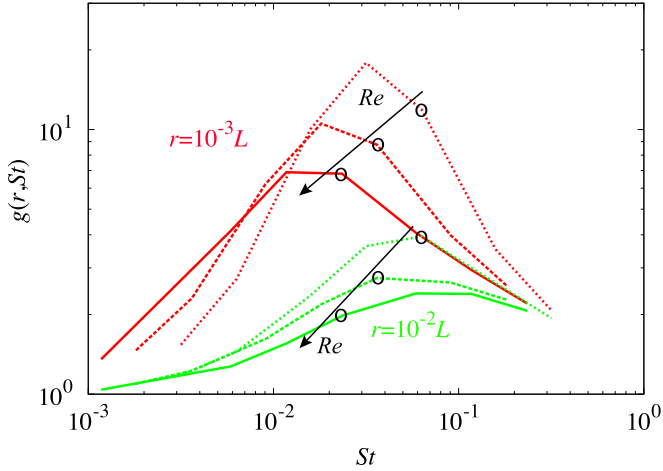

Figure 10. Collision kernel per unit cross-section in spherical formulation at distance $d = 10^{-3}L$ for different Re numbers. The values are measured at $t = 3T$ and normalized by $\langle u^2 \rangle^{1/2}$ for each run. The data from PP13 ($Re = 1000$, $r = \eta/4 \sim 2 \times 10^{-3}L$) are also plotted for comparison.

Figure 9. St dependence of the RDFs at $r = 10^{-3}L$ (red) and $2 \times 10^{-3}L$ (green) for different Re numbers: $Re = 16,100$ (solid line), $Re = 6700$ (dashed line), and $Re = 2100$ (dotted line). The circles denote the data for $St_\eta = 2.0$.

Figure 11. Collision kernel per unit cross-section in spherical formulation at the distance of $\eta/4$ for particle pairs with fixed Stokes ratios, $f \equiv St_2/St_1 = 1$, $1/2$, $1/5$, and 0. The data are obtained at $t = 3T$ in the DNS of $Re = 16,100$. The data from PP15 ($Re = 1000$, $r = \eta/4 \sim 2 \times 10^{-3}L$) are also plotted for comparison.

Ireland et al. (2016) showed that, for fixed values of $St_\eta \gtrsim 1$ and r/η, $g(r)$ is an increasing function of Re. Their Re dependence does not contradict the results in Figure 9. In fact, our DNS data also give almost the same Re dependence as that shown in Figure 21 of Ireland et al. (2016). However, it should be noted that the collision statistics for fixed values of St_η and r/η are completely different from those for fixed values of St and r/L.

Figure 10 presents the Re dependence of the resulting collision kernel obtained by our DNS. In Figure 10, we see a noticeable increase in the collision kernel in the small St range with increasing Re. For example, the value of the collision kernel at $St = 2 \times 10^{-2}$ for $Re = 16,100$ is six times larger than that for $Re = 1000$. However, the Reynolds number dependence of the collision kernel at $St \approx 0.02$–0.2 seems to converge provided that $Re \gtrsim 10^4$. From this finding, it is expected that the collision kernel at $St \approx 0.02$–0.2 for a much higher Reynolds number ($Re \gg 10^4$) is similar to that obtained by our DNS of $Re = O(10^4)$.

As for bidisperse cases, the $St(=St_1)$ dependence of the collision kernel (Equation (14)) is presented for different $f = St_2/St_1$ in Figure 11. To compare the collision kernel at the scale of the smallest eddies, we show the results at the distance
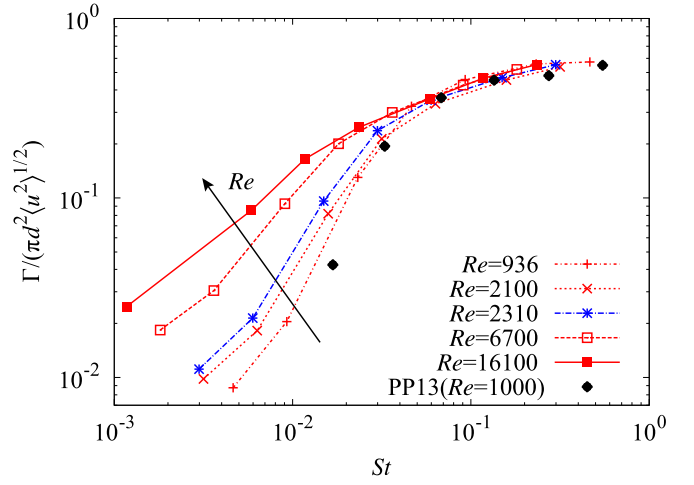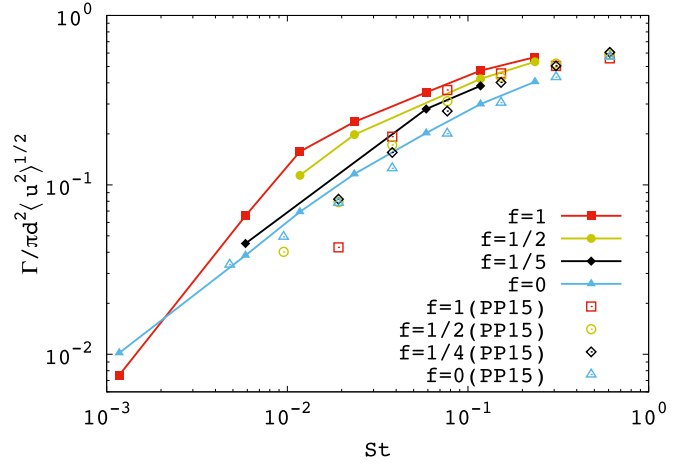
of $\eta/4$. As seen in this figure, the values of Γ for different-sized particles are smaller than those for the identical particles. This result is caused by the fact that the concentration of particles due to turbulent clustering occurs more effectively for identical particles than for different-sized particles. The comparison with the data from PP15 shows that the DNS results for $St \gtrsim 0.1$ at $Re = 16,100$ are not far from those at $Re = 1000$.

3.5. PDF of the Radial Relative Velocity

In the collision kernel, we have adopted the average value of the radial relative velocities, $\langle |w_r| \rangle$. However, to assess the fraction of particles that have velocities lower than the critical collision velocity, we should derive the PDF of w_r. Since the critical collision velocity may be different between equal-sized collisions and different-sized ones, we need to obtain the PDF depending on the Stokes number ratio $f \equiv St_2/St_1$.

Based on the DNS data of $Re = 16,100$, we acquire the PDF for equal-sized particles, $P^{(\mathrm{eq})}$. Figure 12 shows the resultant PDF of the normalized radial relative velocity w_r/U at a
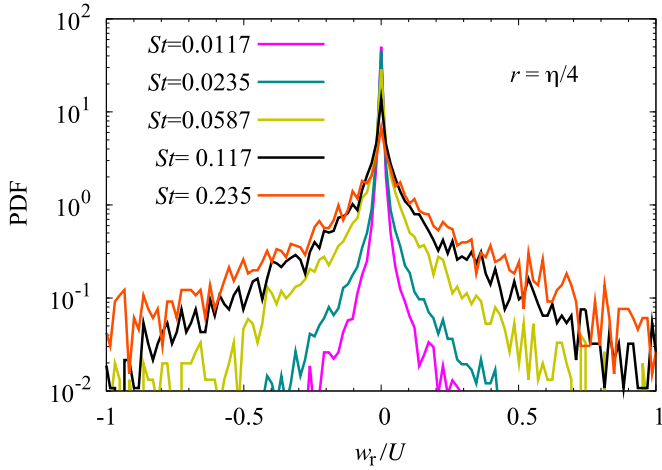
Figure 12. PDF of the normalized radial component of the relative velocity for each St. The relative velocities are measured at $t = 3T$ for the pairs of equal-sized particles at a separation of $r = \eta/4$ in the DNS of $Re = 16{,}100$.

separation of $r = \eta/4$ for each St number, where U is the rms value of the fluctuating velocity in one direction. The negative and positive values of w_r/U represent the approaching and receding pairs, respectively. The variance and kurtosis of $x \equiv w_r/U$ are defined as

$$V \equiv \langle (x - \langle x \rangle)^2 \rangle \tag{16}$$

and

$$K \equiv \langle (x - \langle x \rangle)^4 \rangle / \langle (x - \langle x \rangle)^2 \rangle^2, \tag{17}$$

respectively, and listed in Table 2. It is shown that when $St \geqslant 1.17 \times 10^{-2} (St_\eta \geqslant 1.0)$, the variance is an increasing function of St, and the kurtosis is a decreasing function of St. The data in Table 2 indicate that the values of V and K are respectively approximated as

$$V \approx St^{1.3} \text{ and } K \approx 3.0 + 0.79 \times St^{-1.3} \tag{18}$$

in the range $5.87 \times 10^{-2} \leqslant St \leqslant 2.35 \times 10^{-1}$.

The PDFs for different-sized particles, $P^{(\mathrm{diff})}$, are shown for $f \equiv St_2/St_1 = 1$, $1/2$, and $1/4$, fixing $St_1 = 0.235$, in Figure 13. As expected, Figure 13 suggests that the non-Gaussianity of the PDFs is weakened as f decreases (as the size difference becomes large). A similar trend has already been observed in low-Re simulations (see, e.g., Figures 2, 4, and 8 in Pan et al. 2014b). Our DNS results confirm that the trend is also true for higher-Re turbulence. The variance and the kurtosis of the PDFs for different-sized particles ($f \neq 1$) are listed in Table 3. The data in Tables 2 and 3 imply that, as f decreases, the value of K monotonically decreases while the variance monotonically increases.

Following Sundaram & Collins (1997), Wang et al. (2000), PP13, and Pan et al. (2014b), we attempt to fit the PDF of $x = w_r/U$ with a stretched exponential function given by

$$P_{\mathrm{se}}(x) = \frac{\mu}{2\beta\Gamma(1/\mu)} \exp\left[-\left(\frac{|x|}{\beta} \right)^\mu \right], \tag{19}$$

where $P_{\mathrm{se}}(x)$ is normalized to satisfy $\int_{-\infty}^{\infty} P_{\mathrm{se}}(x)dx = 1$ as in PP13 and Pan et al. (2014b). For this function, the variance and

Table 2
Variance and Kurtosis of the Normalized Relative Velocity (w_r/U) Measured at $t = 3T$ for Equal-sized Particles with a Separation $r = \eta/4$ in the DNS of $Re = 16{,}100$

$St(St_\eta)$	0.0117 (1.0)	0.0235 (2.0)	0.0587 (5.0)	0.117 (10.0)	0.235 (20.0)
Variance (V)	8.04E–4	2.58E–3	2.21E–2	6.15E–2	1.39E–1
Kurtosis (K)	283	85.4	34.1	13.8	8.33
μ	0.273	0.352	0.453	0.632	0.813
β	1.72E–5	3.17E–4	4.75E–3	3.32E–2	1.01E–1

Note. The parameters μ and β in Equation (19), determined using $K_{\mathrm{se}} = K$ and $V_{\mathrm{se}} = V$, are also listed.
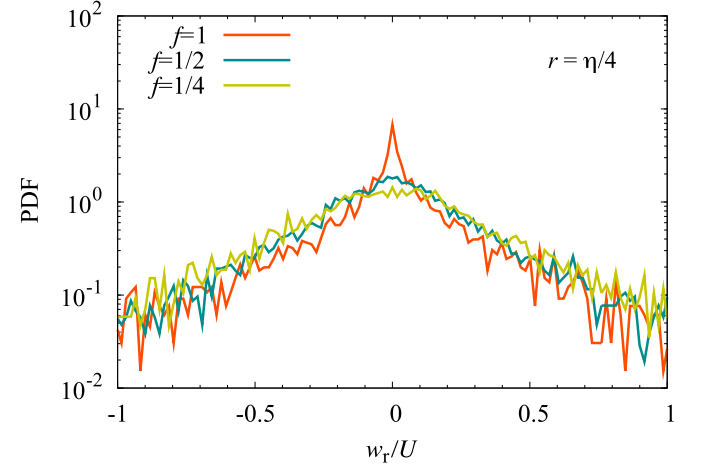

Figure 13. Same as Figure 12 but for pairs of different-sized particles St_1 and St_2, where $St_1 = 0.235$ and $f = St_2/St_1$.

Table 3
Same as Table 2 but for Pairs of Different-sized Particles

f	1/2	1/4	1/2
$St_1(St_{\eta 1})$	0.117(10.0)	0.235(20.0)	0.235(20.0)
$St_2(St_{\eta 2})$	0.0587(5.0)	0.0587(5.0)	0.117(10.0)
Variance (V)	8.91E–2	1.74E–1	1.50E–1
Kurtosis (K)	9.40	5.13	7.03
μ	0.760	1.12	0.899
β	0.069	0.203	0.130

Note. The value of f denotes the ratio St_2/St_1.

kurtosis are analytically given by

$$V_{\mathrm{se}} = \beta^2 \Gamma(3/\mu)/\Gamma(1/\mu) \tag{20}$$

and

$$K_{\mathrm{se}} = \frac{\Gamma(1/\mu)\Gamma(5/\mu)}{\Gamma(3/\mu)^2}, \tag{21}$$

respectively. Since the value of K_{se} does not depend on the value of β, we can first determine the value of μ with $K_{\mathrm{se}} = K$ and then the value of β with $V_{\mathrm{se}} = V$, where V and K are the DNS values. Specifically, the formula to determine the values of μ and β is given by

$$K_{\mathrm{se}} = K, \quad \beta = \left[\frac{\Gamma(1/\mu)V}{\Gamma(3/\mu)} \right]^{1/2}, \tag{22}$$

where V and K are given by the approximated formulas (Equation (18)). The values of μ and β determined by the DNS for the case $Re = 16,100$ are shown in Tables 2 and 3.

Theoretically, a stretched exponential PDF with $\mu = 4/3$ was predicted for inertial range particles under the assumption of exactly Gaussian flow velocity and Kolmogorov scaling (Gustavsson et al. 2008; PP13). The values of μ for the inertial range particles of $St = O(0.1)$ in our DNS are less than the theoretical value and suggest that the non-Gaussian behavior of the flow velocity affects the PDF of the radial relative velocity of the inertial range particles. Hence, the fitting function (Equation (19)) and the values of μ and β in Tables 2 and 3 are useful for modeling the PDF of the radial relative velocities for the inertial range particles. Note that the values of μ for the particles of $0.1 < St < 0.3$ in our DNS are not far from those for the corresponding St values reported for low-Re simulations in Pan et al. (2014b). This fact suggests that not only the variance but also the PDF of the normalized relative velocity for $St \gtrsim 0.1$ is not so sensitive to the values of the Reynolds number.

An example of the stretched exponential fit to the PDF is plotted in Figure 14(a) for the case of identical particles. We confirm that the stretched exponential function qualitatively approximates well the PDFs of the relative velocities. In Figure 14(b), we show the accuracy of the fitting quantitatively by evaluating the integral $Q(x) \equiv \int_{-x}^{x} P^{(eq)}(x) dx$.

4. Implications for Planetesimal Formation

The density of compact dust aggregates is virtually equal to that of a monomer ($\rho_s \approx 1\ \mathrm{g\ cm^{-3}}$). The formation of centimeter-sized ($St = 0.01$–0.1) compact aggregates (pebbles) is key to the growth to planetesimals via streaming instability (e.g., Johansen et al. 2014). On the other hand, dust aggregates can have fluffy structures with much lower bulk densities if the compression due to impacts is sufficiently weak (Okuzumi et al. 2009; Wada et al. 2009; Zsom et al. 2010, 2011; Okuzumi et al. 2012). In recent years, the collisions of fluffy dust aggregates have been explored by performing N-body molecular dynamics simulations (Paszun & Dominik 2009; Wada et al. 2009; Meru et al. 2013; Seizinger & Kley 2013; Wada et al. 2013; Gunkelmann et al. 2016). These studies have revealed that fluffy aggregates, depending on the breaking energy, may resolve the difficulties due to bouncing and fragmentation barriers. So far, fluffy aggregates are thought to likely form as a result of the coalescence of icy grains. However, quite recently, Arakawa & Nakamoto (2016) have shown that fluffy aggregates can result from the collisions of nanometer-sized silicate grains. Here, according to Johansen et al. (2014), we consider two cases of compact aggregates with $\rho_s = 1\ \mathrm{g\ cm^{-3}}$ and extremely fluffy aggregates with $\rho_s = 10^{-5}\ \mathrm{g\ cm^{-3}}$.

As for a protoplanetary disk, we assume an α-model, in which the turbulent viscosity is given as $\nu_t = \alpha c_s H$, c_s is the sound speed, H is the vertical scale height, and the typical value of α is between $\sim 10^{-4}$ to 10^{-2}. In addition, we employ the MMSN model (Hayashi 1981), which provides the gas temperature $T_g = 280(R/\mathrm{au})^{-1/2}$ K, the gas density $\rho_g = 1.2 \times 10^{-9}\ (R/\mathrm{au})^{-11/4}\ \mathrm{g\ cm^{-3}}$, the sound speed $c_s = 1.1 \times 10^3 (R/\mathrm{au})^{-1/4}\ \mathrm{m\ s^{-1}}$, the surface mass density of gas $\Sigma_g = 1.7 \times 10^3 (R/\mathrm{au})^{-3/2}\ \mathrm{g\ cm^{-2}}$, and the vertical scale height of the gas $H = 4.7 \times 10^{-2}(R/\mathrm{au})^{5/4}$ au, where R is the distance from the central star. Assuming a cross-section of $2.5 \times 10^{-15}\mathrm{cm^2}$ for hydrogen molecules, we have the kinematic
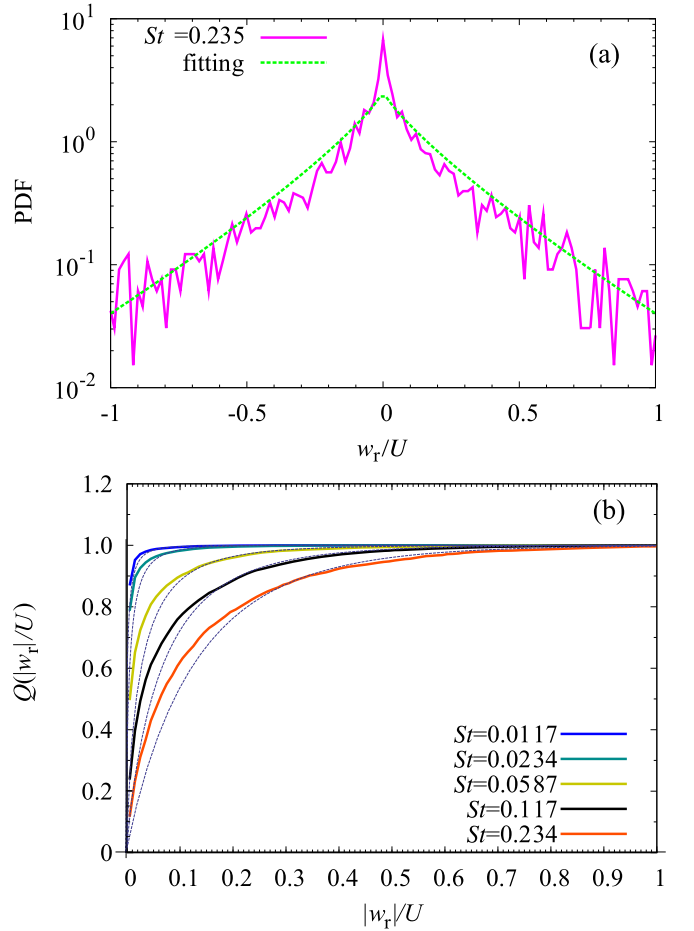

Figure 14. (a) Comparison between the PDF of the normalized radial relative velocities for $St = 0.235$ at a separation of $r = \eta/4$ and the fitting function (Equation (19)). (b) Values of the integral $Q(x) \equiv \int_{-x}^{x} P^{(eq)}(x) dx$ (solid lines) for different St, where $x = |w_r|/U$ and $P^{(eq)}(x)$ is the PDF from the DNS of $Re = 16,100$. The data are compared with $\int_{-x}^{x} P_{se}^{(eq)}(x) dx$ (dotted lines), where $P_{se}^{(eq)}(x)$ is given by Equation (19), in which the values of β and μ in Table 2 are used.

Table 4
Turbulence Characteristics in the α-models of the Protoplanetary Disk at $R = 1$ au

α	U (m s^{-1})	L (m)	Re	η (m)	τ_η (s)
10^{-2}	110	5.5×10^8	10^{10}	17	50
10^{-4}	11	5.5×10^7	10^8	54	500

viscosity given by $\nu = 6.0 \times 10^4 (R/\mathrm{au})^{5/2}\ \mathrm{cm^2\ s^{-1}}$. In the α-model, the characteristic velocity and the characteristic length scale in the turbulence are given by $U = \alpha^{1/2} c_s$ and $L = \alpha^{1/2} H$, respectively, i.e., $U = 1.1 \times 10^2 (\alpha/10^{-2})^{1/2}(R/\mathrm{au})^{-1/4}\ \mathrm{m\ s^{-1}}$ and $L = 5.5 \times 10^8 (\alpha/10^{-2})^{1/2}(R/\mathrm{au})^{5/4}$ m. Thus, the Reynolds number is given by $Re = UL/\nu \sim 10^{10}(\alpha/10^{-2})(R/\mathrm{au})^{-3/2}$ and the Kolmogorov length and timescale are estimated using $\eta = Re^{-3/4}L$ and $\tau_\eta = Re^{-1/2}(L/U)$. The turbulence characteristics for $\alpha = 10^{-2}$ and 10^{-4} are listed in Table 4.

4.1. Collision Velocity in the MMSN Model

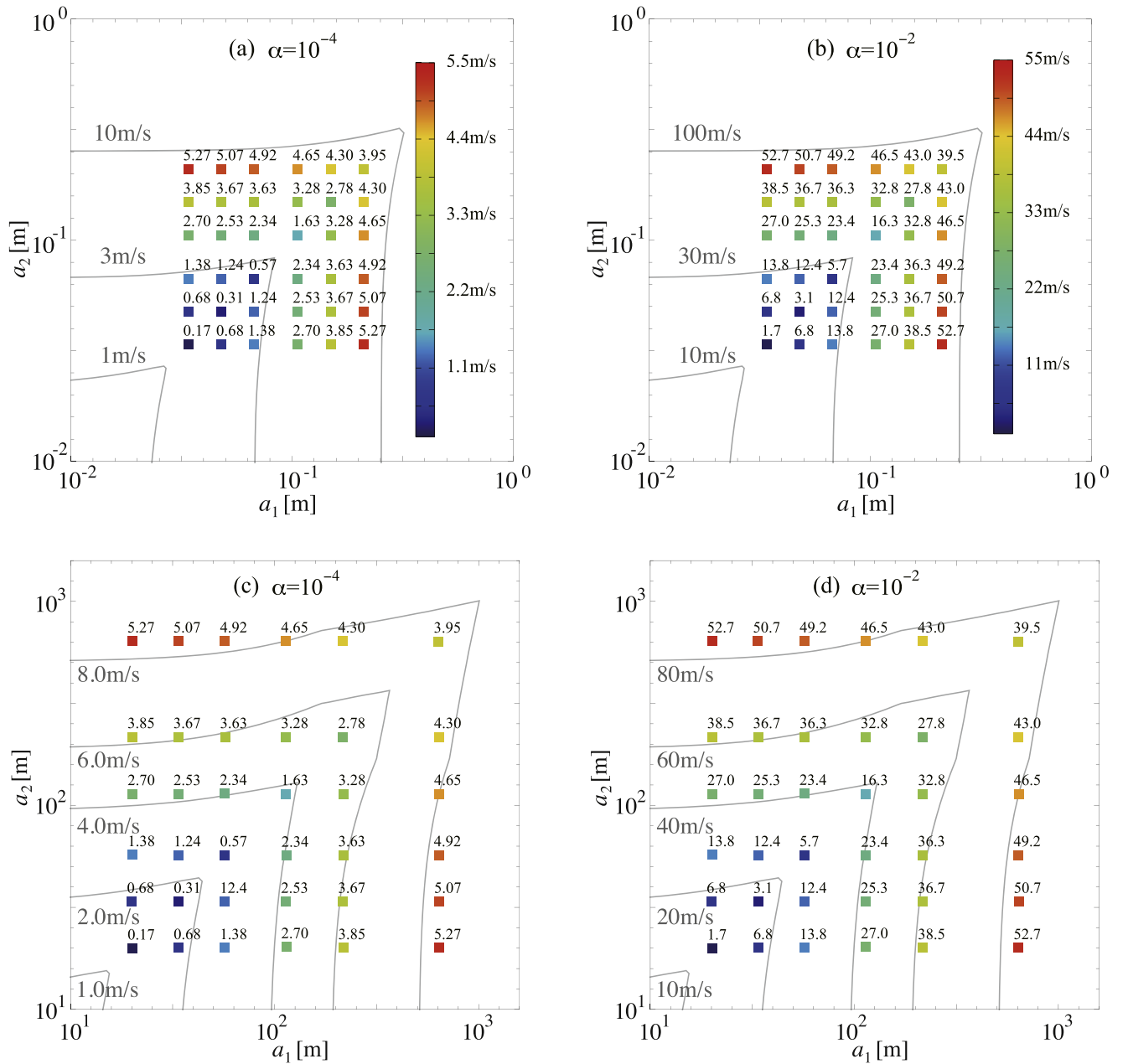Based on the MMSN model, we evaluate the rms relative velocities induced by turbulence. In Figure 6, we showed the

Figure 15. rms relative velocities (in m s^{-1}) between two particles of different sizes for compact aggregates ($\rho_s = 1$ g cm^{-3}; top panels) and fluffy aggregates ($\rho_s = 10^{-5}$ g cm^{-3}; bottom panels). Here, the MMSN model is employed assuming 1 au from the central star for (a), (c) $\alpha = 10^{-4}$ and (b), (d) $\alpha = 10^{-2}$. Filled squares (with rms values) represent the DNS results, while the contours (with rms values) are the theoretical estimates obtained from OC07, using the particle sizes corresponding to the Stokes numbers given by Johansen et al. (2014).

rms relative velocities as a function of St number pairs. Translating the Stokes numbers into particle sizes according to Johansen et al. (2014), we can obtain the rms collision velocities for compact and fluffy dust aggregates. In Figure 15, we show the resultant rms collision velocities at 1 au from the central star, for $\alpha = 10^{-4}$ in panels (a) and (c), and for $\alpha = 10^{-2}$ in panels (b) and (d). The upper panels are the results for compact aggregates, and the lower ones are those for fluffy aggregates. For comparison, the estimates derived with the closed-form analytic formula by OC07 are also depicted. We find that the rms relative velocities by the DNSs are smaller by more than a factor of two, compared to the prediction of the closed-form expression. In particular, for particles of equal size, the DNS results are much lower. These results have a

considerable impact on the sticking rates and the collision timescale as discussed below.

4.2. Sticking Rates of Colliding Pairs

We estimate the "sticking rates," which are defined to be the probabilities of colliding pairs sticking per unit time. Hubbard (2012) pointed out that to estimate the sticking rates of colliding pairs, the weighting factor proportional to the collision rate should be taken into account. In the cylindrical kernel formulation, the collision rate is proportional to $|\boldsymbol{w}|$, and the collision-rate-weighted distribution of the 3D amplitude is obtained from the unweighted PDF, $P(|\boldsymbol{w}|)$, simply as

$$P_{\mathrm{cyl}}(|\boldsymbol{w}|) = |\boldsymbol{w}|P(|\boldsymbol{w}|)/\langle|\boldsymbol{w}|\rangle. \qquad (23)$$
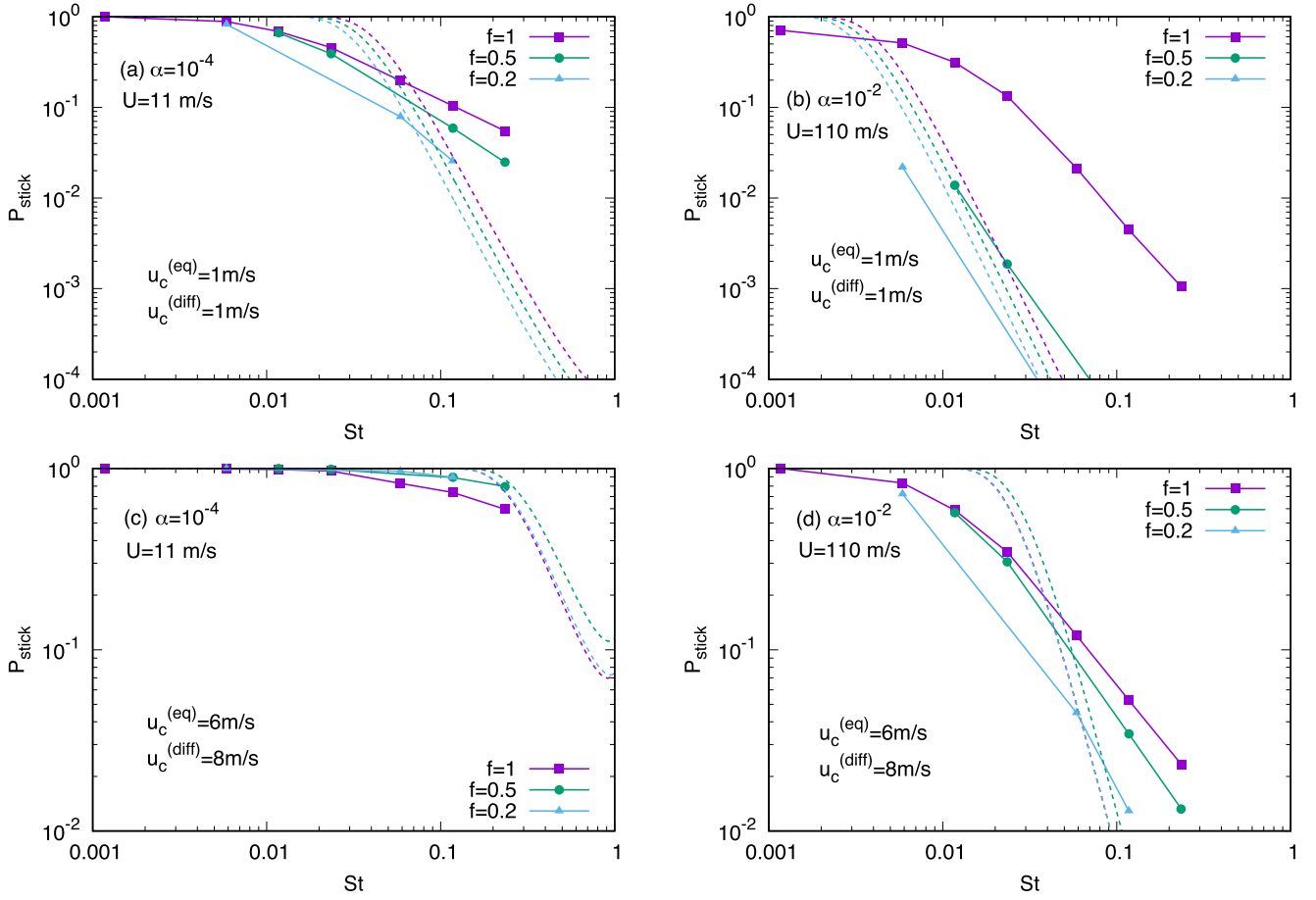
Figure 16. Sticking rates of colliding particles as a function of St, depending on $f = St_2/St_1$. The MMSN model is employed, assuming 1 au from the central star for (a), (c) $\alpha = 10^{-4}$ ($U = 11$ m s^{-1}) and (b), (d) $\alpha = 10^{-2}$ ($U = 110$ m s^{-1}). In the top panels (a) and (b), the critical collision velocity is assumed to be $u_c^{(eq)} = u_c^{(diff)} = 1$ m s^{-1}, while in the bottom panels (c) and (d), this is $u_c^{(eq)} = 6$ m s^{-1} for equal-sized collisions and $u_c^{(diff)} = 8$ m s^{-1} for different-sized collisions, which are given for silicate dust by Wada et al. (2013). Colored solid curves represent the DNS results calculated from the PDFs, using pairs of particles at a separation $r = \eta/4$ in the DNS of $Re = 16,100$. Colored dotted curves denote the theoretical prediction assuming a Gaussian (Maxwell) distribution whose variance is given by OC07.

As shown in Pan & Padoan (2014), the spherical kernel formulation of the weighted PDF is also possible but is more complicated. Therefore, we use Equation (23) for estimating the sticking rates, which are given by

$$P_{stick}^{(eq,\ diff)} = \int_0^{u_c^{(eq,diff)}} P_{cyl}^{(eq,diff)}(x)\,dx \qquad (24)$$

for equal-sized and different-sized collisions, respectively, where $x = |w|$ and u_c is the critical velocity above which the collisions lead to bouncing or fragmentation (see, e.g., Wada et al. 2013).

Wada et al. (2009), using N-body molecular dynamics simulations, have obtained the critical velocity for silicate aggregates to be $u_c = 1.1(a/0.76\ \mu\mathrm{m})^{-5/6}$ m s^{-1}, where a is the size of monomers in aggregates. It agrees well with laboratory experiments (Blum & Wurm 2000). Additionally, Wada et al. (2013) have derived a scaling relation of the critical collision velocity as a function of the breaking energy. They have considered fluffy aggregates composed of ballistic particle-cluster aggregation clusters, which are fairly compact (fractal dimension $D \sim 3$). Even in such compact aggregates, all surface interactions between monomers in contact in the aggregates determine the critical collision velocity, which depends on the size of the monomers. For icy aggregates, they

have derived the critical collision velocity as

$$u_c^{(eq)} = 60(a/\mu\mathrm{m})^{-5/6}\ \mathrm{m\ s^{-1}}, \qquad (25)$$

$$u_c^{(diff)} = 80(a/\mu\mathrm{m})^{-5/6}\ \mathrm{m\ s^{-1}}, \qquad (26)$$

for collisions between equal-sized and different-sized particles, respectively, and for silicate aggregates,

$$u_c^{(eq)} = 6(a/\mu\mathrm{m})^{-5/6}\ \mathrm{m\ s^{-1}}, \qquad (27)$$

$$u_c^{(diff)} = 8(a/\mu\mathrm{m})^{-5/6}\ \mathrm{m\ s^{-1}}. \qquad (28)$$

Recently, Gunkelmann et al. (2016) studied the porosity dependence of the fragmentation of fluffy aggregates composed of silicate grains with radius of 0.76 μm, and found that the critical velocity for agglomerate fragmentation decreases with the porosity of the aggregates. Although the critical collision velocities are still under debate, those for silicate aggregates are smaller by an order of magnitude than those for icy aggregates. Therefore, the sticking rates are expected to be much lower in silicate aggregates. Here, we consider two cases of u_c for silicate aggregates: $u_c = 1$ m s^{-1} for compact aggregates and Equations (27) and (28) for fluffy aggregates.

We evaluate the sticking rates of $P_{stick}^{(eq)}$ and $P_{stick}^{(diff)}$ assuming $R = 1$ au for the cases with $\alpha = 10^{-4}$ and 10^{-2}, based on the
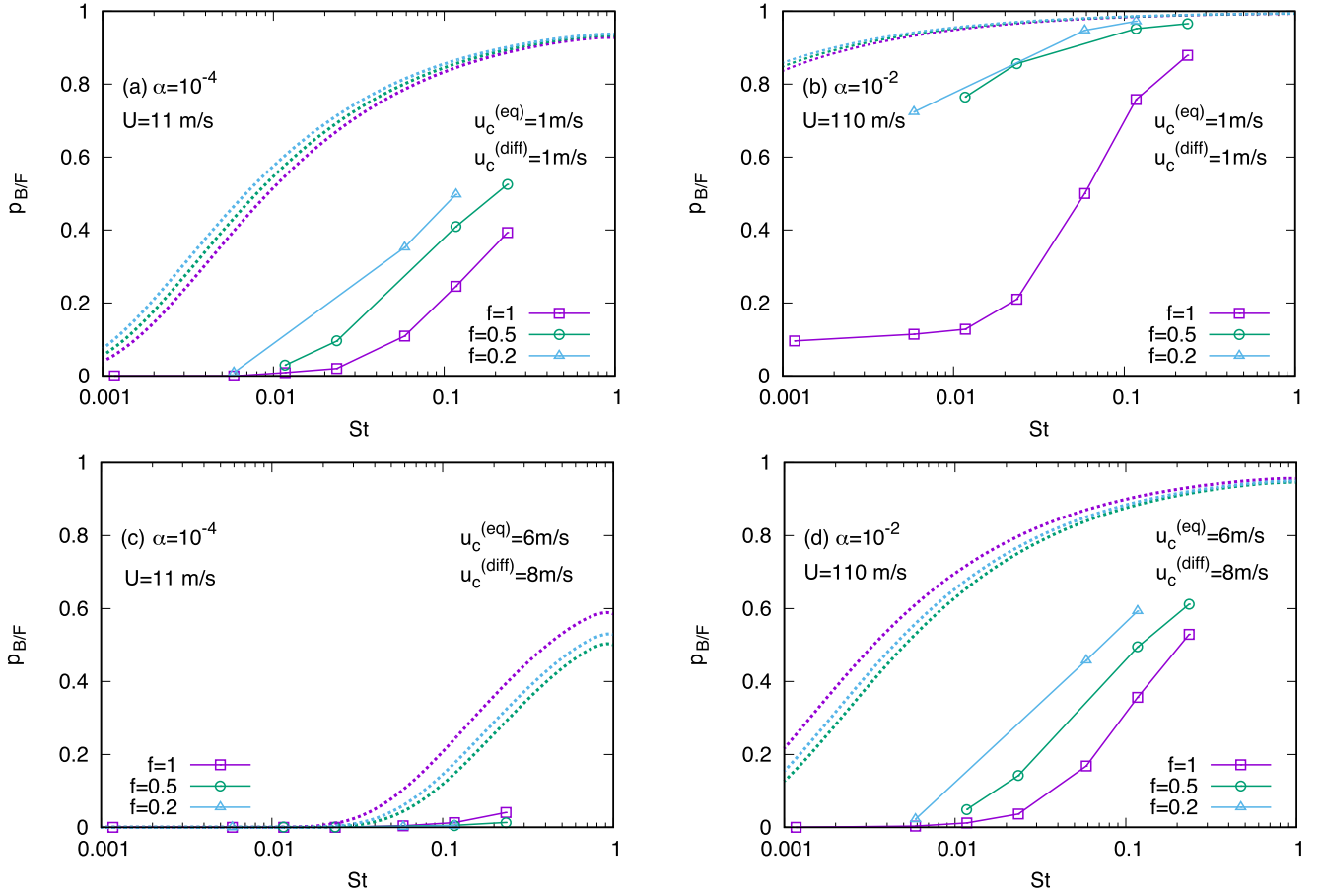
Figure 17. Bouncing/fragmentation probabilities of colliding particles as a function of St, depending on $f = St_2/St_1$. The meanings of the curves are the same as those in Figure 16.

PDFs obtained by the DNS with $Re = 16{,}100$. In Figure 16, we plot the results as a function of St. For comparison, we also plot the theoretical prediction based on the collision-rate-weighted distribution of the 3D amplitude assuming a Gaussian (Maxwell) distribution with the variance given by OC07.

Panels (a) and (b) show, respectively, the DNS results for $\alpha = 10^{-4}$ and 10^{-2}, assuming $u_c = 1 \text{ m s}^{-1}$. Quite interestingly, the sticking rates are not strongly dependent on α if $St \lesssim 0.01$ and remain at a high level of $\gtrsim 50\%$, although the theoretical prediction from a Gaussian distribution declines steeply for $\alpha = 10^{-2}$. Besides, the decrease of the rates at $St \gtrsim 0.01$ is much more gradual compared to the theoretical prediction, especially in the case of $\alpha = 10^{-2}$. It shows that the non-Gaussianity of the velocity distribution function due to turbulent clustering makes the sticking rates for $St \gtrsim 0.01$ remarkably higher than those theoretically expected. Also, it is worth noting that the rates for equal-sized particles ($f = 1$) are higher than those for different-sized particles ($f \neq 1$). In the case of $\alpha = 10^{-2}$, the difference is more than an order of magnitude. This comes from the fact that the variance of the relative velocities is smaller for equal-sized particles ($f = 1$), as shown in Figure 15. These results imply that equal-sized particles grow much faster than different-sized particles, and therefore the fraction of equal-sized particles increases with time.

Panels (c) and (d) show, respectively, the DNS results for $\alpha = 10^{-4}$ and 10^{-2}, assuming the critical collision velocity for fluffy aggregates given by Wada et al. (2013). In panel (c), the

Table 5
Maximal Density Contrast of Dust Particles as a Function of the Stokes Number (St)

ΔL $[\alpha^{1/2} H]$	St				
	0.0117	0.0234	0.0587	0.117	0.234
0.16	1.89	2.46	3.92	5.12	6.01
0.32	1.45	1.76	2.63	3.49	4.00
0.64	1.23	1.36	1.56	1.88	2.30

Note. ΔL is a coarse-grain scale in units of $\alpha^{1/2}H$, where the density is calculated in the volume of ΔL^3.

DNS results show that the sticking rates are approximately unity at $St \lesssim 0.03$, and also that the sticking rates are slightly higher for different-sized particles ($f \neq 1$). As shown in Figure 13, the PDFs have small differences for different f values. However, $u_c^{(\text{diff})}$ is larger than $u_c^{(\text{eq})}$, and therefore $P_{\text{stick}}^{(\text{diff})}$ is a bit higher than $P_{\text{stick}}^{(\text{eq})}$. But, in the case of $\alpha = 10^{-2}$, the rates for $f = 1$ are higher than those for $f \neq 1$ and decline more gradually compared to the theoretical prediction at $St \gtrsim 0.01$.

4.3. Bouncing/Fragmentation Probabilities

Using the PDFs, we can evaluate the bouncing/fragmentation fraction of colliding particles, if we specify the critical collision velocity u_c as in the previous subsection. The

13

Table 6
Collision Timescale of Dust Particles Defined as $t_{coll} \equiv 1/[n_d g(r) \langle |w_r| \rangle \sigma]$, where $n_d (= \rho_d / m_d)$ is the Number Density of the Dust Particles with the Radius a (ρ_d is the Dust Density in the Disk and m_d the Mass of the Dust Aggregate), $g(r)$ is the RDF of the Particle, $\langle |w_r| \rangle$ is the Average of the Radial Relative Velocities, and $\sigma (= \pi (2a)^2)$ is the Cross-section Area

St	Compact ($\rho_s = 1$ g cm^{-3})					Fluffy ($\rho_s = 10^{-5}$ g cm^{-3})				
	0.0117	0.0235	0.0587	0.117	0.235	0.0117	0.0235	0.0587	0.117	0.235
a [cm]	4.36	6.17	9.75	13.8	19.5	1379	1950	3083	4361	6167
m_d [kg]	0.347	0.982	3.88	11.0	31.1	110	311	1228	3473	9823
t_{coll}[yr]	1.07	1.01	1.07	1.12	1.32	0.00338	0.00319	0.00337	0.0035	0.00418

Note. The timescale is shown for compact aggregates ($\rho_s = 1$ g cm^{-3}) and fluffy aggregates ($\rho_s = 10^{-5}$ g cm^{-3}).

bouncing/fragmentation probabilities are estimated as

$$p_{B/F}^{(eq,diff)} = \int_{-\infty}^{-u_c^{(eq,diff)}/U} P^{(eq,diff)}(x) dx \qquad (29)$$

for equal-sized and different-sized collisions, respectively, where $x = w_r/U$.

We evaluate the B/F (bouncing/fragmentation) probabilities of $p_{B/F}^{(eq)}$ and $p_{B/F}^{(diff)}$ assuming $R = 1$ au for the cases with $\alpha = 10^{-4}$ and 10^{-2}, based on the PDFs obtained by the DNS with $Re = 16{,}100$. In Figure 17, we plot the results as a function of St. In any case, the obtained B/F probabilities are significantly lower than the theoretical prediction from a Gaussian distribution. Also, importantly, the B/F probabilities for equal-sized particles ($f = 1$) are much lower than those for different-sized particles ($f \neq 1$). For $St \lesssim 0.01$, the B/F probabilities for $f = 1$ are lower than 10% even in the case of $\alpha = 10^{-2}$. As discussed above, the rms relative velocity in the DNSs is smaller than that in the closed-form expression, and also, the average radial relative velocity is even lower than the rms relative velocity, as shown in Section 3.4. Owing to such low values of relative velocities and the non-Gaussianity of the PDF in the DNSs, the B/F probabilities are not dramatically enhanced even for $\alpha = 10^{-2}$. Hence, equal-sized particles preferentially survive even in a highly turbulent flow.

4.4. Streaming Instability

As shown above, the fluffy silicate aggregates may coalesce with a high probability in a weakly turbulent disk ($\alpha = 10^{-4}$). However, the coagulation of compact aggregates is much less effective for $St \gtrsim 0.1$ in a highly turbulent disk ($\alpha = 10^{-2}$), and hence there is still the obstacle of the radial drift barrier. For the growth from centimeter-sized ($St = 0.01$–0.1) compact aggregates (pebbles) to planetesimals, the streaming instability may be a possible route to circumvent this obstacle.

Youdin & Goodman (2005) discovered the streaming instability promoted by the action-reaction pair of the drag force between solid particles and gas, and the growth of pebbles via streaming instability has been extensively explored (Johansen et al. 2014 and references therein). Importantly, Johansen et al. (2009) and Bai & Stone (2010) have pointed out that there is a critical solid abundance Z_c, above which a spontaneous strong concentration of solids occurs, where Z is the solid-to-gas surface mass density ratio, with $Z \sim 0.01$ being the solar abundance. Using 2D simulations, Carrera et al. (2015) found that the critical abundance is supersolar and increases drastically with decreasing particle size for $St < 0.1$. Very recently, using 2D and 3D high-resolution simulations, Yang et al. (2017) have shown that the critical abundance is not

a steep function of St, and $0.01 < Z_c < 0.02$ for particles of $St = 10^{-2}$, and $0.03 < Z_c < 0.04$ for particles of $St = 10^{-3}$. Although these are slightly supersolar, some mechanisms are still required to enhance the solid abundance to allow the formation of planetesimals via streaming instability.

In our simulations, as shown in Figure 8, the solid abundance is enhanced by turbulent clustering, which is dependent on St. Since the clustering is dependent on scales, the density contrast of dust particles, $\rho_d/\bar{\rho}_d$, depends on a coarse-grain scale. In Table 5, we show the maximal density contrast of dust particles as a function of St, where ΔL is a coarse-grain scale in units of $\alpha^{1/2}H$, and the density is calculated in the volume of ΔL^3. As seen in Table 5, the enhancement of solid abundance becomes larger as St increases and L decreases. If $\alpha = 10^{-2}$ and $\Delta L \leqslant 0.03H$, the enhancement is a factor of ~ 1.5 for $St = 0.01$ and ~ 3.5 for $St = 0.1$. This satisfies the condition for critical abundance shown in Figure 9 of Youdin & Goodman (2005).

As shown in Figure 16, the sticking of equal-sized particles is faster than that of different-sized ones. This supports the assumption of particles of the same size employed by Yang et al. (2017). The sticking rate of equal-sized particles is as high as $\gtrsim 50\%$ at $St \lesssim 0.01$, and reduces to $\lesssim 10\%$ at $St \gtrsim 0.1$, in the case of $\alpha = 10^{-2}$. Furthermore, Figure 17 shows that the B/F probabilities are as low as $\lesssim 10\%$ at $St \lesssim 0.01$, and increase steeply toward $St \gtrsim 0.1$. Therefore, equal-sized particles of $St \sim 0.01$ are expected to selectively grow.

Also, we evaluate the collision timescale of dust particles, which is given by $t_{coll} \equiv 1/[n_d g(r) \langle |w_r| \rangle \sigma]$, where n_d is the number density of the dust particle of size a, $g(r)$ is the RDF of the particle, $\langle |w_r| \rangle$ is the averaged radial relative velocity, and $\sigma (= \pi (2a)^2)$ is the cross-section area. Note that the collision timescale is independent of the value of α, since $n_d \propto \alpha^{-1/2}$ and $\langle |w_r| \rangle \propto \alpha^{1/2}$. As for $g(r)$ and $\langle |w_r| \rangle$, we use the values at $r/\eta = 1/4$ for $Re = 16{,}100$. If we specify the values of St and ρ_s, we have n_d and a in the Stokes regime, using the vertical scale height for dust particles (Okuzumi et al. 2012). In Table 6, the evaluated collision times are listed for compact aggregates ($\rho_s = 1$g cm^{-3}) and fluffy aggregates ($\rho_s = 10^{-5}$ g cm^{-3}). Since $g(r)$ is a decreasing function of St and $\langle |w_r| \rangle$ is an increasing function, the collision timescale is insensitive to St and much shorter than the drift timescale even for compact aggregates.

Considering the above assessments, we can expect that mostly equal-sized particles of $0.01 \lesssim St \lesssim 0.1$ grow in a timescale of $\sim \Omega^{-1}$. Simultaneously, turbulent clustering enhances the solid abundance. According to Yang et al. (2017), the critical solid abundance tends to be minimal toward $St \sim 0.1$. Hence, the streaming instability may be triggered at

$0.01 < St < 0.1$, and the strong concentration of solids proceeds on a timescale of $\gtrsim 100 \; \Omega^{-1}$.

5. Conclusions

In order to investigate the dynamical statistics of dust particles through turbulent clustering in a protoplanetary disk, we have performed high-resolution DNSs of the NS equations. The number of grid points and the Reynolds number are up to 2048^3 and $Re = 16,100$, respectively, which are of the highest resolution ever in astrophysical DNSs. These large-scale DNSs have allowed us to track the motion of dust particles with Stokes numbers of $0.01 \lesssim St \lesssim 0.2$ in the inertial range for the first time.

As a result of these simulations, we found the following:

1. As the Reynolds number of the turbulence increases (or the inertial range widens), the rms relative velocity, $\langle w^2 \rangle^{1/2}$, of particle pairs at a fixed small separation (normalized by the integral length scale) is augmented for small St number particles and is asymptotically proportional to $St^{1/2}$ in the inertial range.
2. The rms relative velocities from the DNSs are smaller by more than a factor of two compared to those from the closed-form expression derived by Ormel & Cuzzi (2007), irrespective of the St number ratios of the particle pairs. Also, the averaged radial relative velocity is even lower than the rms relative velocity. Hence, the findings by Pan & Padoan (2013, 2015) have been confirmed by high-Re DNSs.
3. The PDFs of the radial relative velocities are highly non-Gaussian and are well fitted by a stretched exponential function like Equation (19). The PDF of the normalized relative velocity for $St \gtrsim 0.1$ is not so sensitive to the values of the Reynolds number. Hence, the results are consistent with those at low-Re by Pan et al. (2014b).
4. Almost independently of α, the sticking rates of colliding particles are as high as $\gtrsim 50\%$ for particles of $St \lesssim 0.01$ and declines gradually at $St \gtrsim 0.01$, although the theoretical prediction from a Gaussian distribution declines steeply for $\alpha = 10^{-2}$. This comes from the non-Gaussianity of the radial relative velocities and the smaller variance of the relative velocities as a result of the turbulent clustering.
5. Since the variance of the relative velocities for equal-sized particles ($f = 1$) is smaller than that for different-sized particles ($f \neq 1$), the sticking rates for $f = 1$ are higher than those for $f \neq 1$. The difference is larger than an order of magnitude in the case of $\alpha = 10^{-2}$. It implies that equal-sized particles grow much faster than different-sized particles, and therefore the fraction of equal-sized particles increases with time.
6. The B/F probabilities are significantly lower than the theoretical prediction from a Gaussian distribution. The probabilities for equal-sized particles ($f = 1$) are much lower than those for different-sized particles ($f \neq 1$), in the case of $\alpha = 10^{-2}$. Hence, equal-sized particles preferentially survive even in a highly turbulent flow.
7. Turbulent clustering enhances the solid abundance. The enhancement on a scale of 0.03 scale heights of the disk increases by a factor of ~ 1.5 at $St = 0.01$ to ~ 3.5 at $St = 0.1$, in the case of $\alpha = 10^{-2}$. Therefore, streaming instability may be triggered at $0.01 < St < 0.1$.

In the present DNSs, we have assessed sticking rates, but the actual coagulation of dust particles has not been incorporated. Hence, we cannot predict the mass function of dust aggregates as a result of the hierarchical coagulation. This is a significant issue for planetesimal formation. In DNSs in the near future, we will explore the growth of dust aggregates in turbulence.

ORCID iDs

Takashi Ishihara (ID) https://orcid.org/0000-0002-4520-6964

References

Adachi, I., Hayashi, C., & Nakazawa, K. 1976, PThPh, 56, 1756
Arakawa, S., & Nakamoto, T. 2016, ApJL, 832, L19
Bai, X.-N., & Stone, J. M. 2010, ApJ, 722, 1437
Birnstiel, T., Dullemond, C. P., & Brauer, F. 2009, A&A, 503, L5
Birnstiel, T., Klahr, H., & Ercolano, B. 2012, A&A, 539, A148
Blum, J., & Wurm, G. 2000, Icar, 143, 138
Blum, J., & Wurm, G. 2008, ARA&A, 46, 21
Bragg, A. D., & Collins, L. R. 2014, NJPh, 16, 055014
Brauer, F., Dullemond, C. P., & Henning, T. 2008a, A&A, 480, 859
Brauer, F., Henning, T., & Dullemond, C. P. 2008b, A&A, 487, L1
Carrera, D., Johansen, A., & Davies, M. B. 2015, A&A, 579, A43
Chiang, E., & Youdin, A. N. 2010, AREPS, 38, 493
Cuzzi, J. N., & Hogan, R. C. 2003, Icar, 164, 127
Davila, J., & Hunt, J. 2001, JFM, 440, 117
Donzis, D. A., Yeung, P. K., & Sreenivasan, K. R. 2008, PhFl, 20, 045108
Falkovich, G., & Pumir, A. 2007, JAtS, 64, 4497
Fessler, J. R., Kulick, J. D., & Eaton, J. K. 1994, PhFl, 6, 3742
Garaud, P., Meru, F., Galvagni, M., & Olczak, C. 2013, ApJ, 764, 146
Gunkelmann, N., Ringl, C., & Urbassek, H. M. 2016, A&A, 589, A30
Gustavsson, K., & Mehlig, B. 2011, PhRvE, 84, 045304
Gustavsson, K., Mehlig, B., Wilkinson, M., & Uski, V. 2008, PhRvL, 101, 174503
Güttler, C., Blum, J., Zsom, A., Ormel, C. W., & Dullemond, C. P. 2010, A&A, 513, A56
Hayashi, C. 1981, PThPS, 70, 35
Hubbard, A. 2012, MNRAS, 426, 784
Ida, S., & Guillot, T. 2016, A&A, 596, L3
Ireland, P. J., Bragg, A. D., & Collins, L. R. 2016, JFM, 796, 617
Ishihara, T., Enohata, K., Morishita, K., Yokokawa, M., & Ishii, K. 2015, in PaCT 2015, Parallel Computing Technologies, Vol. 9251, ed. V. Malyshkin (Cham: Springer), 522
Ishihara, T., Kaneda, Y., Yokokawa, M., Itakura, K., & Uno, A. 2007, JFM, 592, 335
Ishihara, T., Morishita, K., Yokokawa, M., Uno, A., & Kaneda, Y. 2016, PhRvF, 1, 082403
Jimenez, J., Wray, A., Saffman, P., & Rogallo, R. 1993, JFM, 255, 65
Johansen, A., Blum, J., Tanaka, H., et al. 2014, in Protostars and Planets VI, ed. H. Beuther et al. (Tucson, AZ: Univ. Arizona Press), 547
Johansen, A., Youdin, A., & Mac Low, M.-M. 2009, ApJL, 704, L75
Kaneda, Y., Ishihara, T., Yokokawa, M., Itakura, K., & Uno, A. 2003, PhFl, 15, L21
Kataoka, A., Tanaka, H., Okuzumi, S., & Wada, K. 2013, A&A, 557, L4

Kerr, R. M. 1985, JFM, 153, 31
Lissauer, J. J. 1993, ARA&A, 31, 129
Markiewicz, W. J., Mizuno, H., & Voelk, H. J. 1991, A&A, 242, 286
Mattor, N., Williams, T. J., & Hewett, D. 1995, ParC, 21, 1769
Maxey, M. R. 1987, PhFl, 30, 1915
Meru, F., Geretshauser, R. J., Schäfer, C., Speith, R., & Kley, W. 2013, MNRAS, 435, 2371
Okuzumi, S., Tanaka, H., Kobayashi, H., & Wada, K. 2012, ApJ, 752, 106
Okuzumi, S., Tanaka, H., & Sakagami, M.-a. 2009, ApJ, 707, 1247
Ormel, C. W., & Cuzzi, J. N. 2007, A&A, 466, 413
Pan, L., & Padoan, P. 2013, ApJ, 776, 12
Pan, L., & Padoan, P. 2014, ApJ, 797, 101
Pan, L., & Padoan, P. 2015, ApJ, 812, 10
Pan, L., Padoan, P., & Scalo, J. 2014a, ApJ, 791, 48
Pan, L., Padoan, P., & Scalo, J. 2014b, ApJ, 792, 69
Pan, L., Padoan, P., Scalo, J., Kritsuk, A. G., & Norman, M. L. 2011, ApJ, 740, 6
Paszun, D., & Dominik, C. 2009, A&A, 507, 1023
Saffman, P. G., & Turner, J. S. 1995, JFM, 1, 16
Schumacher, J. 2007, EL, 80, 54001
Seizinger, A., & Kley, W. 2013, A&A, 551, A65
Squires, K. D., & Eaton, J. K. 1991, PhFlA, 3, 1169
Sundaram, S., & Collins, L. R. 1997, JFM, 335, 75
Vincent, A., & Meneguzzi, M. 1991, JFM, 225, 1
Völk, H. J., Jone, F. C., Morfill, G. E., & Roeser, S. 1980, A&A, 85, 316
Wada, K., Tanaka, H., Okuzumi, S., et al. 2013, A&A, 559, A62
Wada, K., Tanaka, H., Suyama, T., Kimura, H., & Yamamoto, T. 2009, ApJ, 702, 1490
Wang, L.-P., Wexler, A. S. Q., & Zhou, Y. 2000, JFM, 415, 117
Watanabe, T., & Gotoh, T. 2007, JFM, 590, 117
Weidenschilling, S. J. 1977, MNRAS, 180, 57
Wilkinson, M., Mehlig, B., & Bezuglyy, V. 2006, PhRvL, 97, 048501
Windmark, F., Birnstiel, T., Ormel, C. W., & Dullemond, C. P. 2012, A&A, 544, L16
Yamazaki, Y., Ishihara, T., & Kaneda, Y. 2002, JPSJ, 71, 777
Yang, C.-C., Johansen, A., & Carrera, D. 2017, A&A, 606, A80
Yeung, P. K., & Pope, S. B. 1988, JCoPh, 79, 373
Yeung, P. K., Zhai, X. M., & Sreenivasan, K. R. 2015, PNAS, 112, 12633
Yokokawa, M., Itakura, K., Uno, A., Ishihara, T., & Kaneda, Y. 2002, in SC '02: Proceedings of the 2002 ACM/IEEE Conference on Supercomputing (Los Alamitos, CA: IEEE Computer Society Press), 50
Youdin, A. N., & Goodman, J. 2005, ApJ, 620, 459
Zsom, A., Ormel, C. W., Dullemond, C. P., & Henning, T. 2011, A&A, 534, A73
Zsom, A., Ormel, C. W., Güttler, C., Blum, J., & Dullemond, C. P. 2010, A&A, 513, A57